A Data-Driven Neural Network Model to Correct Derived Features in a RANS-based Simulation of the Flow Around a Sharp-Edge Bluff Body

by

Seyedamir Shojaee

a thesis submitted in partial fulfilment of the requirements for the degree of

master of science

Department of MECHANICAL ENGINEERING

University of Alberta

ABSTRACT

In this dissertation, a machine-learning method is utilized to enhance the accuracy of wake parameters calculated by Reynolds Averaged Navier Stokes (RANS) $k-\omega$ SST model of flow on and around wall-mounted rectangular cylinders. Using high-quality results from Large Eddy Simulation (LES), this correction method at Reynolds number of 2.5×10^3 saves computational cost and time, while yielding more accurate wake parameters.

The performance of $k-\omega$ SST model to predict the mean wake characteristics and mean global parameters is evaluated in comparison to LES results of the flow around wall-mounted rectangular cylinders. The comparison reveals the inaccuracy of $k-\omega$ SST model to predict these characteristics. Different cylinder aspect ratios are considered with depth ratios ranging from 1 to 4 at 0.5 increments. To correct the prediction accuracy of the $k-\omega$ SST model, a backpropagation multi-layer perceptron artificial neural network is developed, introduced and tested.

The qualitative and quantitative comparison of the results of LES and $k-\omega$ SST model show that the fundamental properties of flow features over wall-mounted rectangular cylinders, including shear-layer separation, recirculation, and reattachment, are successfully captured by the $k-\omega$ SST model. In addition, the $k-\omega$ SST model accurately predicts wake topologies, including the tip, base, and horseshoe vortices. However, the global features of the mean flow, mean wake structures, and mean flow features differ significantly from the LES results.

The neural network was effectively trained using reliable data to improve the accuracy of the mean wake features and global parameters simulated by $k-\omega$ SST model. These features and parameters are the reattachment length (X_R) behind the cylinder, recirculation length (X_F) in front of the cylinder, top recirculation length (X_T) on the top surface of the cylinder, mean drag coefficient ($\overline{C}_d$), mean lift coefficient ($\overline{C}_l$), and mean base pressure coefficient ($\overline{C}_{bp}$). Furthermore, the trained algorithm correctly predicted unobserved data in addition to the given data, which demonstrates the robustness of the developed correction algorithm.

PREFACE

All the simulations, data analysis and interpretation of results in this thesis were performed by Seyedamir Shojaee under the supervision of Dr. Carlos Lange and Dr. Arman Hemmati. The simulations are completed using the resources of the Digital Research Alliance of Canada.

To my parents, my eldest brother, and my love

for your endless love, support, and encouragement

ACKNOWLEDGEMENTS

First and foremost, I would like to express my most profound appreciation to my supervisors, Dr. Carlos Lange and Dr. Arman Hemmati, for their continuous support, encouragement, and advice. Their immense knowledge and guidance indeed enriched my research skills and provided me with the opportunity to accomplish my MSc thesis. I am also grateful to my friends, colleagues and research team for their invaluable suggestions and the cherished time spent together that made my study and life in Canada a wonderful time.

This endeavour would not have been possible without the support and motivation of my brother, Dr. Nima Shojaee, whose insights always inspire me throughout my life. Also, words cannot express my gratitude to my parents, my brothers, and my wife (Kiana) for always being there for me through the ups and downs of my life. Without their love, I have nothing in my life. I also appreciate all the support I received from the rest of my family.

Finally, I would like to extend my sincere thanks for the generous financial support of this work from the Natural Sciences and Engineering Research Council of Canada (NSERC), Alberta Innovates and Canada First Research Excellence.

Contents

List of Tables

List of Figures

LIST OF ABBREVIATIONS, SYMBOLS, AND NOMENCLATURE

Latin Symbols

h	cylinder height
d	cylinder width
l	cylinder length
Re	Reynolds number
Re_d	Reynolds numebr based on width (d)
k	turbulence kinetic energy
U_0	free-stream or bulk velocity
t	time
t^*	convective time
u	Cartesian $x-$wise velocity component
v	Cartesian $y-$wise velocity component
w	Cartesian $z-$wise velocity component
p	pressure
X_R	recitculation length behind the cylinder
X_T	recitculation length at the top of the cylinder
X_F	recitculation length front of the cylinder
C_d	drag coefficient
C_l	lift coefficient
C_{bp}	base pressure coefficient
h_θ	hypothesis function
J_θ	cost function

Greek Symbols

δ	Boundary layer thickness
ε	Turbulent kinetic energy dissipation rate
ω	Turbulence specific dissipation rate
τ	Stress tensor
τ_w	Wall Shear Stress
η	Kolmogorov length scale
ρ	density
μ	dynamic viscosity
ν	kinematic viscosity

Other Symbols

∇	Gradient operator
$\overline{\square}$	Mean (time-averaged)
∂	Partial derivative
$\square \cdot \square$	Dot product
Δ	Difference
$\approx$	i approximately
$[\ ]^T$	Transpose
$O[\ ]$	Order of

Abbreviations

2D	Two Dimensional
3D	Three Dimensional
AR	aspect ratio
DR	depth ratio
CFD	Computational Fluid Dynamics
FVM	Finite Volume Method
DNS	Direct Numerical Simulation
LES	Large Eddy Simulation
DES	Detached Eddy Simulation
RANS	Reynolds Averaged Navier Stokes
SST	Shear Stress Transport
PIV	Particle Image Velocimetry
LDA	Laser Doppler Anemometery
CFL	Courant-Friedrichs-Levy Number
SGS	Sub-Grid Scale
SIMPLE	Semi-Implicit Method for Pressure Linked Equations
PISO	Pressure Implicit with Splitting of Operators
ML	Machine Learning
ANN	Artificial Neural Network
BP	Back-Propagation
MLP	Multi-Layer Perceptron
$LSTM - RNN$	Long-Short-Term-Memory Recurrent Neural Network
CNN	Convolutional Neural Networks
ELM	Extreme Learning Machine

SVM	Support Vector Machine
LMA	Levenberg-Marquardt Algorithm
GNA	Gauss-Newton Algorithm

Chapter 1

INTRODUCTION

1.1 The Overview

Turbulent flows are the most common type of flow in both natural and practical applications. The movement of natural gas and oil in pipelines, the growth of boundary layers on aircraft wings, and the majority of combustion processes all involve turbulence and frequently even depend on it. Water in rivers and canals moves in turbulent currents, while vehicles, aircraft, and submersibles all leave turbulent wakes behind them (Tennekes and Lumley, 1972). The wake is defined as the extended flow zone with a velocity deficit left behind bluff bodies (Von Kármán, 1963). Da Vinci (ca. 1513) is credited with writing the earliest description of the flow forming around stationary bluff bodies submerged in a water stream. The wake of bluff bodies constitutes a classical problem in fluid mechanics with different engineering applications that can be found in a variety of fields, such as flow past bluff bodies in civil and wind engineering (Tominaga, 2015), heat exchange in the manufacturing of industrial equipment, and even in electronic chips (Rastan et al., 2017). Further, analyzing the behaviour of fluids over bluff bodies is crucial for the design and optimization of civil structures, aircraft systems, and mechanical engineering devices. Some specific examples are wind turbine masts, powerlines, pipelines, buildings, trucks, and heat exchangers. To better understand the flow characteristics around bluff bodies and the development of vortical flow structures, a

substantial amount of research has been done in recent years. This has resulted in significant advancements in our understanding of how fluids and structures interact. According to Williamson (Williamson, 1996b,a, 1997), there are three types of classifications for bluff bodies, based on (1) kinematics of the body, such as stationary, vibrating, or flapping objects; (2) on the geometry of the bluff body, including two or three dimensions, and cylindrical or non-cylindrical; (3) flow regimes, such as laminar or turbulent.

In the case of non-cylindrical and stationary bluff bodies, the flow characteristics behind wall-mounted, sharp-edged bluff bodies have been examined in both experimental (Castro and Robins, 1977; Hassan et al., 2015) and numerical (Cheng et al., 2003; Yakhot et al., 2006; Saha, 2013; da Silva et al., 2020) approaches. Particle Image Velocimetry (PIV) and Laser Doppler Velocimetry (LDV) are two precise experimental techniques utilized for these studies. However, they are restricted to a certain range of Reynolds numbers and test section sizes. For reliable analyses of complicated flow properties, however, numerical approaches offer a well-established platform (Hemmati et al., 2018; Rastan et al., 2021). Flow characteristics of wall-mounted rectangular cylinders can be complex and depend on a variety of factors, such as the cross-sectional shape (Uffinger et al., 2013), aspect ratio (Sakamoto and Arie, 1983; Saha, 2013; Sumner et al., 2017), depth-ratio (Joubert et al., 2015; Rastan et al., 2021), Reynolds number (Zhang, 2017; Wang and Lam, 2019), and boundary layer thickness (Wang et al., 2006; Hosseini et al., 2013). In order to accurately predict these flow characteristics using numerical methods, it is important to use high-precision techniques, such as Large Eddy Simulation (LES) (da Silva et al., 2020; Rastan et al., 2021) or Direct Numerical Simulation (DNS) (Zhang, 2017; Zargar et al., 2022). However, these methods can be computationally expensive and may not be practical for all applications. In such cases, Reynolds Averaged Navier-Stokes (RANS) (Zhang, 2017) equations may be a more practical approach. However, the accuracy of RANS predictions can be limited, especially at high Reynolds numbers or in complex flows. The experimental works of Castro and Robins (1977) and Martinuzzi and Tropea (1993) on a wall-mounted square cylinder were followed by several numerical studies that investigated the performance of RANS turbulence models compared to LES

(Rodi, 1997). RANS simulations can model the flow features to a certain order of accuracy, which requires significant improvements. Modifying the RANS formulation can vary depending on the specific characteristics of the problem. There are many approaches that have been proposed to improve the accuracy of RANS predictions, including: first, modifying the RANS-based turbulence modeling formulations using high-precision results (Hoffman, 1975; Shimada and Ishihara, 2002; Mohamed and Wood, 2017; Liu et al., 2017); second, using hybrid RANS/LES methods that combine the computational efficiency of RANS with the improved accuracy of LES based on spatial (regional) divisions (Roy et al., 2003; Durbin and Baeder, 2013); third, using machine learning techniques to improve the accuracy of RANS predictions. By "learning" from high-precision data, a machine learning model can potentially make more accurate predictions than a traditional RANS model (Ling et al., 2016; Yarlanki et al., 2012; Zhao et al., 2020; Luo et al., 2020; Huijing et al., 2021). The use of machine learning algorithms in regression problems has emerged as a research hotspot in the field of machine learning with the growth of artificial intelligence and the development of new machine learning technologies (Huang et al., 2020). Research on integrated learning has recently attracted the interest of industry and academia, including data mining, pattern identification, medical diagnosis, and scientific research. The basic goal of integrated learning is to use the training data set to teach a variety of separate learners and then to aggregate the outcomes of each prediction into the final result (Huang et al., 2020). The history of the machine learning and fluid mechanics interaction is long and may perhaps be unexpected (Brunton et al., 2020). In the early 1940s, Kolmogorov regarded turbulence as one of the primary application areas of the statistical learning theory (Kolmogorov, 1941). There were two key developments that marked machine learning advancements in the 1950s and 1960s. We may distinguish between machines, such as the perceptron (Rosenblatt, 1958) that attempts to automate procedures, i.e., classification and regression on the one hand, and cybernetics (Wiener, 1965) and expert systems aiming to replicate the thought process of the human brain on the other. The usage of perceptrons sparked a lot of attention. At the outset, the single-layer perceptron could only solve linear problems. However, a multi-layer perceptron that could learn nonlinear functions was presented in 1969 (Minsky and

Papert, 1969). To reduce the error of the system, it was required to calculate the discrepancy between the predicted and actual values. Thus, the backpropagation method was introduced in 1986 to evaluate the errors of each layer in the neural network from the output layer to the first one (Rumelhart et al., 1986). There are many machine learning algorithms that could potentially be applied in this context, including linear regression, decision trees, and artificial neural networks, among others. It is important to carefully select the appropriate machine learning algorithm, based on the characteristics of the data and the specific problem. Additionally, it is important to properly evaluate the performance of the machine learning model, for example by using techniques that avoid overfitting to ensure that the model generalizes well to new data.

1.2 Motivations and Objectives

The flow over wall-mounted cylinders has been widely investigated in the past literature due to their relevance in practical engineering applications. These flows are encountered in airflow over rectangular buildings (Zhang, 2017), urban pollutant dispersion in the wind flow (Kavian Nezhad et al., 2022), applied forces on a cooling tower or photovoltaic panels (Fogaing et al., 2019), aerodynamics of trucks and trailers (Zargar et al., 2021), roughness in internal pipe flows (Goswami and Hemmati, 2020), and heat exchange in electronic devices (Rastan et al., 2021). The flow dynamics around wall-mounted bluff bodies are typically complex and require a precise prediction of the flow behaviour (Cheng et al., 2003; Xu et al., 2017). One of the most fascinating challenges in fluid dynamics may involve detecting the flow structures, controlling the heat transfer, and adjusting the flow around bluff bodies because of its extensive industrial applicability. This information is crucial for optimizing the design of industrial machinery and other technologies that deal with flow interactions with bluff bodies. To this end, there exists a knowledge gap on the wake of cylinders in the range of Reynolds number that in relevant to this study with different cylinder sizes. Furthermore, reducing cost and time of calculation is essential due to the significance of the flow characteristics over rectangular cylinders and their widespread application. Aside from producing

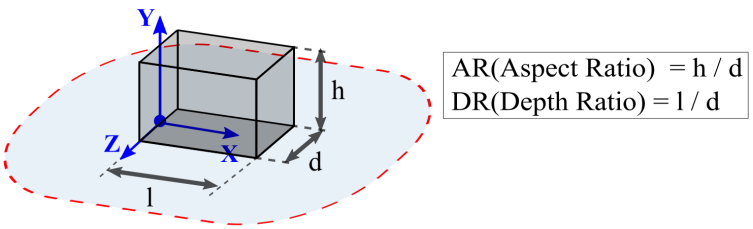

Figure 1.1: Definition of AR and DR with a schematic of a rectangular cylinder.

results that are of higher quality, LES is substantially more expensive than RANS-based simulations. Thus, engineers frequently use RANS turbulence models, particularly for large Reynolds numbers investigations. Based on the studies of Rodi (1997) and Cheng et al. (2003), LES requires significantly more computational resources (about 40–100 times more) than RANS-based simulations, especially for complex flow problems. This is because LES attempts to directly calculate the large-scale, energetic eddies in the flow, while RANS models the effect of these eddies on the mean flow through various approximations. So, LES can provide more accurate predictions of flow characteristics, such as velocity, pressure, and turbulence intensities, but it has a high computational cost. Depending on the specific flow dynamics and the desired level of accuracy, it may be more practical to use RANS rather than LES. Although RANS simulations continue to be the industry standard for low computational demand CFD analysis, these simulations have some drawbacks. For example, they can only provide average quantities and the closure problem is nonlinear, which prevents them from offering the same level of accuracy as LES (Pope, 2000).

The primary objective of this study is to develop a machine-learning algorithm to improve the parameter-specific accuracy of the near-wake characteristics and applied forces simulated by RANS for a wall-mounted rectangular cylinder at all sizes, representing engineering and urban applications. Initially, this thesis investigates the effects of aspect ratio (AR) and depth ratio (DR) (see Figure 1.1) of rectangular cylinders on the performance of RANS simulation based on LES results. This is followed by the development of a machine-learning algorithm that corrects RANS results for specific wake parameters to the same accuracy as LES. There are no extensive studies on the data-driven machine learning algorithm for enhancing these results for rectangular cylinders with different sizes.

Particularly, the first objective is identifying the wake topology from the LES results at $\mathrm{Re}_d = 2.5 \times 10^3$, along with understanding the behaviour of the flow with respect to the changing aspect ratio and depth ratio. Thereafter, this study evaluates the discrepancies between RANS and LES simulation results and identifies parameters that lead to limitations for a correct prediction of the wake behind wall-mounted rectangular cylinders using RANS. The second objective is to apply a neural network algorithm in a regression model and train it by the data from RANS and LES to maximize the precision, affordability, and processing time for RANS simulation of the wake parameters behind wall-mounted rectangular cylinders.

1.3 Novelty

The novelty of this study is twofold. First, the current study fills a knowledge gap on the performance of RANS-based simulations for flow over wall-mounted cylinders with changing aspect ratios and depth ratios compared to that of LES. Second, there are no extensive studies on data-driven machine-learning techniques for post-processing of RANS-based simulation results based on high-precision numerical studies, such as LES, that aim to enhance the accuracy of RANS results.

1.4 Structure of the thesis

This thesis begins with a review of the literature and fundamental topics in wake dynamics, Computational Fluid Dynamics, turbulence modelling, and the artificial neural network in Chapter 2. The methodology and procedures for achieving each objective are outlined in Chapter 3. Particularly, an explanation of the numerical setup for RANS and LES simulations, domain and mesh description, and validation and verification of the solvers, mesh, and domain size are provided in Chapter 3. Chapter 4 contains the results for LES, RANS, and theie comparison in simulating the wake features. Further, Chapter 5 represents how the machine learning algorithm transforms the

accuracy level of RANS data to that of LES for the quantitative features of the rectangular cylinder wake. Finally, the conclusions of this research are presented in Chapter 6.

Chapter 2

BACKGROUND

The state of the literature for this thesis is established in this chapter with a brief overview of fundamental and essential topics in fluid dynamics, wake dynamics, CFD, turbulence modeling, and machine learning. For the precise characterization of a fluid condition, various classes were suggested by researches. The most useful categorizations are based on the fluid's viscosity, compressibility, steadiness, and uncertainty. The primary nondimensional governing parameter of the fluid state is identified as the *Reynolds number* (White, 1991):

$$\mathrm{Re} = \frac{\rho u c}{\mu} = \frac{u c}{\nu}, \tag{2.1}$$

where ρ is the fluid density, u is the velocity scale, c is the characteristic length scale, and μ and ν are the fluid's dynamic and kinematic viscosity, respectively. The Reynolds number indicates the ratio of inertial to viscous forces, which corresponds to which of the two primary wake characteristics is dominant.

Viscosity plays a key role in classifying fluid flow as inviscid or viscous. For an inviscid flow, the shear stress components are zero, and the stress tensor has the same components as any other fluid that is stationary. A fluid that experiences internal friction as a result of velocity gradients between adjacent molecules is referred to as viscous fluid (Batchelor and Batchelor, 2000). Another vital fluid characteristic that describes fluid flow is density. A flow where the

fluid density does not change is known as an incompressible flow. Contrary, compressible flows experience changes in density. It is generally accepted that the assumption of incompressible flow is applicable to airflow at a speed less than 30% of the speed of sound (Anderson, 1990).

Unsteady flow is a term used to describe a flow whose properties change over time. Conversely, the flow is referred to as steady flow if the features are independent of time and alter exclusively with spatial variations. In terms of the dynamics of the wake, the transient aspect of the flow is also crucial (Kuethe and Chow, 1997).

Turbulence is one of the unstable flow behaviors that are most frequently investigated but is also one of the least understood. Laminar flows are by definition smooth and regular, such as flows created by slow-moving or viscous fluids (Davidson, 2020). However, there is not comprehensive definition for turbulent flows. In fact, Davidson (2020) argues that the greatest way to identify turbulence is by its characteristics, which include the following:

Irregularity: Because of their random and chaotic nature, turbulent flows are irregular but governed by the Navier-Stokes equations.

Diffusivity: Due to the increased momentum transfer across distinct flow layers in turbulent flow, it has a higher diffusivity than laminar flow.

Dissipativity: The "Energy Cascade" is a method by which turbulence kinetic energy transfers from large scales to smaller scales. By the dominance of viscous forces, the kinetic energy associated with the smallest scales dissipates as heat. Thus, turbulent flow is implied to be dissipative.

Three-Dimensionality: According to the laws underlying vortex dynamics, turbulent flow is inherently three-dimensional. Thus, in a turbulent flow, there are many flow scales or eddies.

Large Reynolds numbers: The level of laminar flow variations and disturbances increases with the Reynolds number.

Continuum: The smallest scales in a turbulent flow are greater than the molecules of the fluid.

The continuity, momentum, and energy equations governed the behavior of the fluid. Depending on the flow, these equations can be simplified. The flow in the current investigation is viscous, incompressible, unsteady, and turbulent, and the governing equations are as (Durbin and Reif,

2011):

$$\frac{\partial u_i}{\partial x_i} = 0 \tag{2.2}$$

$$\rho\frac{\partial u_i}{\partial t} + \rho\frac{\partial u_i u_j}{\partial x_j} = -\frac{\partial p}{\partial x_i} + \mu\frac{\partial^2 u_j}{\partial x_i x_j} + \rho f_i, \tag{2.3}$$

where u is the velocity vector and p is the pressure.

Integral and differential flow characteristics are typically normalized using the flow characteristic length and velocity in order to decrease the complexity of variables. In the current study, bulk velocity (U_0) and cylinder width (d), and length (l) (see Figure 1.1) are used to normalize drag (D) and lift (L) forces, respectively.

$$C_d = \frac{D}{0.5\rho U_0^2 d} \tag{2.4}$$

$$C_l = \frac{L}{0.5\rho U_0^2 l} \tag{2.5}$$

In addition to fluid mechanics, the machine learning method is utilized for various objectives as a tool. Machine learning is the process of training computers to learn as humans do and continuously update and modify their information. Here, the aim is to enhance and optimize their performance systems (Huang et al., 2020). Machine learning methods, such as support vector machines and artificial neural networks, have delivered promising results in a variety of domains, notably fluid mechanics, with the development of artificial intelligence. Depending on the information that the machine learning method has access to regarding the data, the learning algorithms in the field of machine learning can be classified into supervised, and unsupervised learning (Brunton et al., 2020). In supervised learning, a collection of data is provided, and since it is believed that there is a connection between the input and the output, the proper result is already known (Ng, 2020). Further, machine-learning algorithms may be divided into "regression" and "classification" problems. In the former, input variables are mapped to some continuous function in order

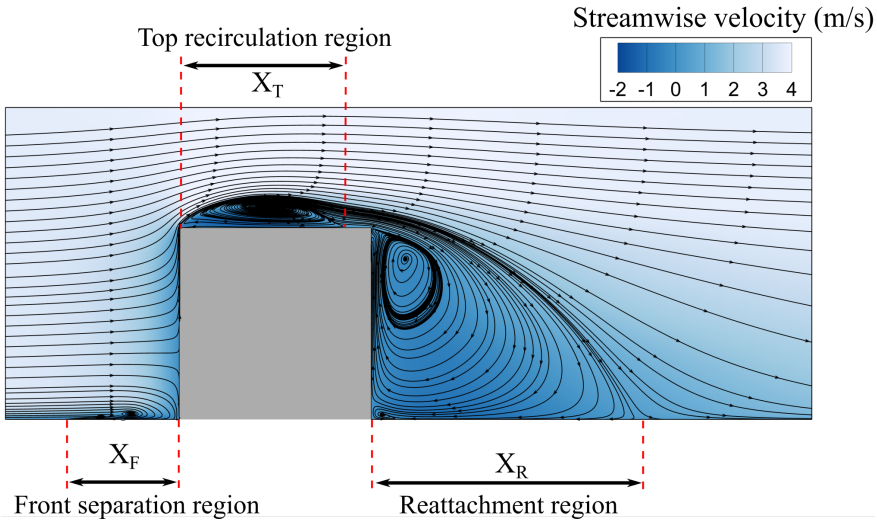

Figure 2.1: Time-averaged velocity streamlines over a wall-mounted cylinder coloured by mean streamwise velocity.

to forecast outcomes within a continuous output. In the latter, results within a discrete output are predicted (Ng, 2020).

2.1 Wake

The flow around bluff bodies, such as a flat plate, cylinder, disc, or sphere, is a well-known and fundamental problem in fluid mechanics. The wake is a region of disturbed flow that is developed behind a bluff body. The recirculating flow region, referred to as the "reattachment length", is formed behind the wall-mounted bluff body (Konstantinidis and Bouris, 2012). Multiple parameters may cause alternation in the size of the wake and wake topology, i.e. the shape and size of the bluff body, lift and drag forces, base pressure (Yu et al., 2013), and Reynolds number (Okajima et al., 1990). The time-averaged (mean) wake features include flow separation, reattachment, and recirculation (Murakami, 1993). The flow dynamics around wall-mounted bluff bodies can be complex and require a precise prediction of the flow behaviour (Cheng et al., 2003; Xu et al., 2017). Figure 2.1 shows the mean wake region formed behind a rectangular cylinder on the plane in the middle of the body, including the reattachment length behind the cylinder (X_R), top recirculation length (X_T), and frontal separation length (X_F) (Martinuzzi and Tropea, 1993).

The flow features behind wall-mounted, sharp-edged bluff bodies have been analyzed in the past literature, both experimentally (Castro and Robins, 1977; Martinuzzi and Tropea, 1993; Wang and Zhou, 2009; Hassan et al., 2015) and numerically (Rodi, 1997; Cheng et al., 2003; Yakhot et al., 2006; Saha, 2013; da Silva et al., 2020; Goswami and Hemmati, 2022). Although experimental methods such as Particle Image Velocimetry (PIV) and Laser Doppler Velocimetry (LDV) are highly accurate, they are limited to a range of Reynolds numbers and the size of the test section. On the other hand, numerical methods provide a well-verified and validated platform for accurate investigations of complex flow features (Hemmati et al., 2018; Rastan et al., 2021; Goswami and Hemmati, 2022). The flow around wall-mounted bluff bodies, such as sharp-edged or circular cylinders, is more complex due to the free-end and cylinder-wall junction effects (Wang et al., 2006). The flow features around the wall-mounted cylinders can be seen in Figure 2.2a, including the generation of free-end tip vortices, wall-body junction engendered base vortices, and mid-span flow structures (Sakamoto and Arie, 1983; Okamoto et al., 1990; Sumner et al., 2004; Wang and Zhou, 2009; Bourgeois et al., 2011; Krajnović, 2011; Porteous et al., 2017; Zhang, 2017). Further, separation and roll-up of the boundary layer in front of the cylinder form a horse-shoe vortex that embraces the cylinder and extends to the wake (Simpson, 2001). These flow features are influenced by the cross-sectional shape (Uffinger et al., 2013; Nguyen et al., 2021), aspect ratio ($AR = h/d$, where h and d are the cylinder height and width respectively) (Sakamoto and Arie, 1983; Wang and Zhou, 2009; Saha, 2013; Sumner et al., 2017; Rastan et al., 2017), depth-ratio ($DR = l/d$, where l is the length of the cylinder) (Joubert et al., 2015; Rastan et al., 2021; Zargar et al., 2021), Reynolds number ($\mathrm{R}e_d = dU_0/\nu$, where U_0 is free-stream velocity and ν is kinematic viscosity) (Zhang, 2017; Zargar et al., 2022; Wang and Lam, 2019; Zhao et al., 2021), and boundary layer thickness (Wang et al., 2006; Hosseini et al., 2013; Hassan et al., 2015; Saeedi and Wang, 2016). The tip and base vortices are associated with the downwash and upwash flow, respectively. The primary tip vortices are generated at the side edges of the cylinder while the secondary tip vortices originate from the leading edge on the top surface of the cylinder (Rastan et al., 2021). The secondary tip vortices disappear rapidly in the downstream wake for high aspect-ratio cylinders (Rastan et al.,

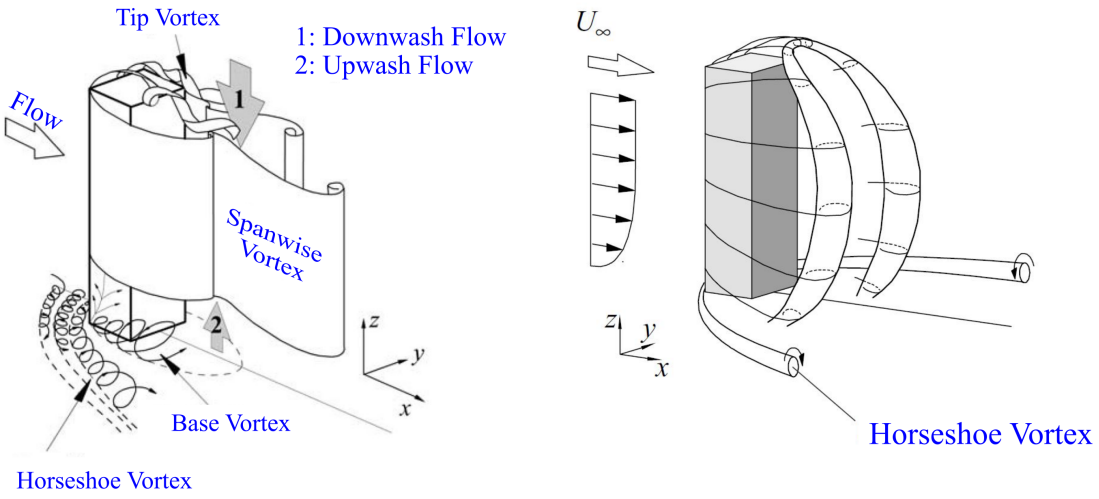

Figure 2.2: The wake topology over a wall-mounted square cylinder represented by (a) Wang et al. (2006) and (b) Wang and Zhou (2009).

2021). Base vortices originate as a pair of counter-rotating vortices from the cylinder-wall junction and are significantly influenced by the thickness of the boundary layer. The symmetric full loop-shape structure is connected to the vortices, such as tip or base vortices, and continues to the downstream wake region refer to as the dipole wake structure. A thin boundary layer weakens the base vortices, which results in a transition from dipole to a no-pole-type cross-sectional wake topology (Hassan et al., 2015; Wang et al., 2006)S. In the span of the cylinder, spanwise Kármán type vortex shedding was observed in the wake (Wang et al., 2006) (Figure 2.2a). Wang and Zhou (2009) proposed that the tip and base vortices were connected inherently to form a single arc-type shedding structure in the wake (Figure 2.2b). Further, Wang and Zhou (2009) showed the existence of symmetric and asymmetric vortex shedding due to periodic or staggered placement of the legs of the formed arches. Furthermore, da Silva et al. (2020) and Goswami and Hemmati (2022) studied the wake behind the cylinder with a range of Reynolds numbers and observed secondary vortex shedding structures formed by the secondary tip vortices. Due to their complex wake dynamics and interactions between the tip, base, and spanwise shedding vortices, the flow around wall-mounted cylinders is an active topic of research.

Sakamoto and Arie (1983) determined the critical aspect ratio which enabled the transition between different mid-span vortex structures. For example, the transition in the mean wake topology from dipole to quadruple wake generally occurred at a critical aspect ratio of 2 for wall-mounted square cylinders (McClean and Sumner, 2014; Sumner et al., 2017; da Silva et al., 2020). For the cases of small aspect ratio ($AR \leq 2$) cylinders at low Reynolds numbers ($\sim 50 - 250$), the intensity of downwash flow suppresses the spanwise vortex shedding (Sakamoto and Arie, 1983; Wang and Zhou, 2009; Rastan et al., 2017; Zargar et al., 2021).

2.2 Computational Fluid Dynamics (CFD)

The foundation of computational fluid dynamics is the numerical solution of the Navier-Stokes equations over multiple initial conditions, assumptions, and flow conditions (Versteeg and Malalasekera, 2007). With the advancement of faster and more reliable computational tools over the past decades, this technique, which was first developed in the early 1930s, has attracted a great deal of attention. Depending on the flow Reynolds number, boundary conditions, physical scales, and non-linear behaviours, CFD simulations can range in scope and accuracy. Due to the complex interactions of wake structures, effective numerical simulation of the flow characteristics in the wake of a wall-mounted cylinder is challenging. Chapter 3 provides a thorough analysis of the solvers and CFD simulation setup used in this thesis.

2.3 Turbulence Modeling

In CFD studies, accurate modelling and simulation of turbulence are crucial, especially when dealing with high Reynolds numbers and complex wakes. The flow around wall-mounted cylinders have been numerically investigated based on DNS (Goswami and Hemmati, 2022; Zargar et al., 2022), LES (Rastan et al., 2021), and RANS simulation (Rodi, 1997; Zhang, 2017). Despite a simple conceptual framework, directly solving the Navier-Stokes equations using DNS is computationally expensive and mostly limited to low Reynolds numbers ($\mathrm{Re} \leq 10^3$) (Moin and Mahesh,

1998). LES enable increasing the Re to moderate to high values ($10^3 - 1.5 \times 10^5$). LES solves the flow by modelling the small scales near the wall using sub-grid scale models, such as Smagorinsky and Dynamic Smagorinsky, while directly calculating the large-scale eddies using spatially filtered Navier-Stokes and continuity equations (Reif and Durbin, 2011). Both LES and DNS simulations, even though numerically accurate, are computationally very expensive, especially for large computational domains (Hemmati et al., 2018). The studies using RANS models extend the range of Reynolds numbers by modelling complex flow features, instead of solving them as in the case of LES and DNS (Hemmati et al., 2018). RANS models approximate the Reynolds stresses using different eddy-viscosity models such as Standard $k-\omega$, Standard $k-\varepsilon$, and $k-\omega$ SST. Reynolds stress and the mean strain rate are linearly connected in the eddy-viscosity hypothesis (Schmitt, 2007). Due to their low computational demands and faster simulation times, RANS simulations are accepted in industries for simulations of practical engineering flow phenomena. However, RANS models are limited in computational accuracy and performance compared to other numerical methods (Pope, 2000). Thus, it becomes important to benchmark the performance of different numerical tools, such as turbulence models, in predicting complex flow dynamics, i.e., wake of wall-mounted sharp-edged bluff bodies. Simulations in this dissertation utilize different turbulence models, LES (Dynamic Smagorinsky) and RANS ($k-\omega$ SST). The details of the formulations are provided here.

2.3.1 Large Eddy Simulations

LES is based on volume-averaged Navier-Stokes equations, while RANS models are based on time-averaged equations (Davidson, 2020). The LES governing equations are based on the spatial filtered incompressible Navier-Stokes (Eq. 2.3) and continuity (Eq. 2.2) equations, where the smaller flow scales or eddies relative to the smallest grid size are modelled and larger eddies are calculated directly. Using OpenFOAM, the filtered continuity (Eq. 2.6) and momentum (Eq. 2.7) formulations are solved:

$$\frac{\partial \widehat{u}_i}{\partial x_i} = 0 \tag{2.6}$$

$$\frac{\partial \widehat{u}_i}{\partial t} + \frac{\partial \widehat{u}_i \widehat{u}_j}{\partial x_j} = -\frac{1}{\rho}\frac{\partial \widehat{p}}{\partial x_i} + \nu \frac{\partial^2 \widehat{u}_j}{\partial x_i x_j} + \frac{\partial \widehat{\tau}_{ij}^{SGS}}{\partial x_j} \tag{2.7}$$

Here, $\widehat{\tau}_{ij}^{SGS}$ represents the sub-grid stress (SGS) tensor, and $\widehat{u}_i$ and $\widehat{p}$ are the filtered resolved velocity and pressure, respectively (Durbin and Reif, 2011):

$$\widehat{\tau}_{ij}^{SGS} = \widehat{u_i u_j} - \widehat{u}_i \widehat{u}_j \ . \tag{2.8}$$

To model the sub-grid scale flow features, the dynamic Smagorinsky method is utilized in modeling the flow. According to the Smagorinsky method, the SGS stress tensor is calculated using the eddy viscosity approach (Durbin and Reif, 2011):

$$\widehat{\tau}_{ij}^{SGS} = -2\nu_{SGS}\widehat{S}_{ij} \tag{2.9}$$

$$\widehat{S}_{ij} = \frac{1}{2}\left(\frac{\partial \widehat{u}_j}{\partial x_i} + \frac{\partial \widehat{u}_i}{\partial x_j}\right) \tag{2.10}$$

$$\nu_{SGS} = (c_s \Delta)^2 \sqrt{2\left|\widehat{S}\right|^2} \tag{2.11}$$

$$\left|\widehat{S}\right| = \widehat{S}_{ij}\widehat{S}_{ji} \tag{2.12}$$

Here, Δ is the cube root of the volume of the cells and $\widehat{S}_{ij}$ is the filtered value of the rate of the strain tensor. In case of the Dynamic Smagorinsky method, value of the Smagorinsky constant (c_s) is calculated in every timestep:

$$c_s^2 = -\frac{L_{ij}m_{ij}}{m_{kl}m_{kl}} \tag{2.13}$$

$$m_{ij} = 2^{\frac{2}{3}}\Delta^2 \widetilde{\left|\widehat{S}_{ij}\right| \widehat{S}_{ij}} - 2^{\frac{2}{3}}\Delta^2 \left|\widetilde{\widehat{S}}_{ij}\right| \widetilde{\widehat{S}}_{ij} \tag{2.14}$$

$$L_{ij} = \widetilde{\widehat{u}_i \widehat{u}_j} - \widetilde{\widehat{u}}_i \widetilde{\widehat{u}}_j \, . \tag{2.15}$$

Here, the tilde sign represents the second filter applied to the flow data and L_{ij} is the Leonard stress. Moreover, by restricting the value of the constant c_s to only positive values, $c_s^2 = max(c_s^2; 0)$, numerical instabilities are prevented.

2.3.2 Reynolds Averaged Navier Stokes

The RANS $k-\omega$ SST model (Menter, 1994) is the combination of the standard $k-\omega$ (Wilcox, 2006) and $k-\epsilon$ model (Jones and Launder, 1972). It and has shown better performance in terms of predictability of flow features in regions of negative pressure gradient (Moukalled et al., 2015). The governing equations following the implementation of Reynolds decomposition and averaging yield the RANS equations:

$$\frac{\partial \overline{\boldsymbol{u_i}}}{\partial x_i} = 0 \tag{2.16}$$

$$\overline{\boldsymbol{u_j}} \frac{\partial \overline{\boldsymbol{u_i}}}{\partial x_j} = -\frac{1}{\rho}\frac{\partial \overline{p}}{\partial x_i} + \nu \frac{\partial \overline{\boldsymbol{u_i}}}{\partial x_i \partial x_j} - \frac{\partial \overline{\boldsymbol{u_i}' \boldsymbol{u_j}'}}{\partial x_j} \tag{2.17}$$

Here, Eq. 2.17 can be rewritten as:

$$\rho \left(\overline{\boldsymbol{u_j}} \frac{\partial \overline{\boldsymbol{u_i}}}{\partial x_j} \right) = \frac{\partial}{\partial x_j} \left[-\overline{p}\delta_{ij} + \mu \left(\frac{\partial \overline{\boldsymbol{u_i}}}{\partial x_j} + \frac{\partial \overline{\boldsymbol{u_j}}}{\partial x_i} \right) - \rho \overline{\boldsymbol{u_i}' \boldsymbol{u_j}'} \right] \tag{2.18}$$

the expression included in square brackets denotes the combination of three stresses: $\overline{p}\delta_{ij}$ from the mean pressure field, viscous stress, and *Reynolds shear stress* ($-\overline{u_i{'}u_j{'}}$), which is defined in a tensor form as:

$$\boldsymbol{\tau_{ij}} \;=\; -\overline{\boldsymbol{u_i{'}u_j{'}}} \;=\; \begin{bmatrix} -\overline{u_x{'}u_x{'}} & -\overline{u_x{'}u_y{'}} & -\overline{u_x{'}u_z{'}} \\ -\overline{u_y{'}u_x{'}} & -\overline{u_y{'}u_y{'}} & -\overline{u_y{'}u_z{'}} \\ -\overline{u_z{'}u_x{'}} & -\overline{u_z{'}u_y{'}} & -\overline{u_z{'}u_z{'}}\ . \end{bmatrix} \tag{2.19}$$

The number of equations does not equal the number of variables, which leads to the problem of closure in turbulence. The τ_{ij} term is modelled using a combination of Boussinesq and Eddy viscosity approximations to "close" the RANS equations (e.g., Eq. 2.18). The methods used to estimate or simulate the stress tensor parameters vary amongst turbulence models and might account for their accuracy or lack thereof.

In this dissertation, the two-equation $k-\omega$ SST turbulence model is employed, using OpenFOAM. The turbulence model initial conditions and transport equations, as implemented in OpenFOAM (OpenCFD, 2019), are described below. Turbulence models are solved using the Semi-Implicit Method for Pressure-Linked equations (SIMPLE) algorithm for pressure-velocity coupling, which allows steady-state approximations of governing equations using an iterative procedure.

Initial Conditions

According to Vold (2017), the following formulas can be used to determine the turbulent kinetic energy (k) for isotropic turbulence:

$$k \;=\; \frac{3}{2}(I\ \ u_\infty)^2, \tag{2.20}$$

Here, u_∞ is the free-stream velocity, and I is the turbulence intensity. Further, the turbulence dissipation rate (ε) can be estimated by:

$$\varepsilon \;=\; \frac{{C_\mu}^{\frac{3}{4}}\;\; k^{\frac{3}{2}}}{L}, \tag{2.21}$$

Here, L is the turbulent length scale and given as 0.22 of the inlet boundary layer thickness for this study, and C_μ is a model constant equal to 0.09. Finally, the turbulence-specific dissipation rate (ω) is estimated by:

$$\omega \;=\; \frac{{C_\mu}^{\frac{-1}{4}}\;\; k^{\frac{1}{2}}}{L}\,. \tag{2.22}$$

Standard k$-\varepsilon$ Model

The turbulence kinetic energy equation in the Standard k$-\varepsilon$ turbulence model is given as (Cappelli and Mansour, 2013):

$$\frac{\partial}{\partial x_i}(k\overline{\boldsymbol{u_i}}) \;=\; \frac{\partial}{\partial x_i}\left(\frac{\nu_t}{\sigma_k}\frac{\partial k}{\partial x_i}\right) \;+\; P_k \;-\; \varepsilon, \tag{2.23}$$

and the turbulence kinetic energy dissipation rate is defined by:

$$\frac{\partial}{\partial x_i}(\varepsilon\overline{\boldsymbol{u_i}}) \;=\; \frac{\partial}{\partial x_i}\left(\frac{\nu_t}{\sigma_\varepsilon}\frac{\partial \varepsilon}{\partial x_i}\right) \;+\; \frac{C_1\varepsilon}{k}\left(P_k + C_3\frac{2}{3}k\frac{\partial \boldsymbol{u_i}}{\partial x_i}\right) \;-\; C_2\frac{\varepsilon^2}{k}\,. \tag{2.24}$$

Here, ν_t is the eddy viscosity, defined as $\nu_t = C_\mu\frac{k^2}{\varepsilon}$, and C_1, C_2, C_3, σ_k and σ_ε are model closure coefficients, the values for which are:

$$C_1 = 1.44;\;\; C_2 = 1.92;\;\; C_3 = 0.0;\;\; \sigma_k = 1.0;\;\; \sigma_\varepsilon = 1.3. \tag{2.25}$$

Standard $k-\omega$ Model

For the Standard $k-\omega$ model, the equation for the turbulence-specific dissipation rate (ω) is presented in Eq.2.26, the transport equation for k stays the same as Eq. 2.23:

$$\frac{\partial}{\partial x_i}(\omega\overline{\boldsymbol{u_i}}) \;=\; \frac{\partial}{\partial x_i}\left[(\nu+\alpha_\omega\nu_t)\frac{\partial\omega}{\partial x_i}\right] \;+\; \alpha\frac{\omega}{k}\nu_t P_k \;-\; \beta\omega^2 \;+\; \frac{2\nu_t}{\sigma_{\omega k}}\frac{\partial\omega}{\partial x_i}\frac{\partial k}{\partial x_i} \tag{2.26}$$

Here, the closure model coefficients are:

$$\alpha_\omega = 0.5;\;\; \alpha = 0.52;\;\; \beta = 0.072. \tag{2.27}$$

$k-\omega$ SST Model

The $k-\omega$ and $k-\varepsilon$ models are combined to form the $k-$ Shear Stress Transport model, or SST. The flow simulation uses the $k-\omega$ model in the region close to the wall and the $k-\varepsilon$ model in the fully turbulent areas away from the walls. The transport equations for k and ω are kept the same as Eqs. 2.23 and 2.26 respectively, but extra closure coefficients are added to correctly model the last term of Equation 2.26 (Cappelli and Mansour, 2013):

$$\begin{aligned} &\alpha_{\omega 1} = 0.5; \quad \alpha_{\omega 2} = 0.856; \quad \alpha_{k1} = 0.85; \\ &\alpha_{k2} = 1; \qquad \beta_1 = 0.072 \;\; ; \quad \beta_2 = 0.0828; \\ &\beta^* = 0.09; \quad a_1 = 0.31; \qquad b_1 = 1. \end{aligned} \tag{2.28}$$

RANS Modification

The aforementioned RANS turbulence models have limitations due to modeling of the closure problem. To reduce the error of prediction, there have been several investigations on the comparison of RANS simulation with relevant higher precision experiments.

Previous numerical and experimental studies have focused on the two-dimensional, infinite-span (Okajima et al., 1990; Nakagawa et al., 1999) or circular cross-section cylinder (Sumner et al., 2004) while recent studies have focused on finite wall-mounted cylinders. Shah and Ferziger (1997) numerically studied the flow over a wall-mounted cube at $\mathrm{Re}_d = 4 \times 10^4$ using LES and showed a satisfactory comparison with experimental results of Castro and Robins (1977) and Martinuzzi and Tropea (1993). Further, Rodi (1997) numerically studied the performance of LES and RANS-based turbulence models in predicting the flow around a wall-mounted cube, similar that of Shah and Ferziger (1997). Similar investigations were carried out by Lübcke et al. (2001) using RANS and LES at $\mathrm{Re}_d = 2.2 \times 10^4$ and Roy et al. (2003) using different RANS models and hybrid RANS/LES models at $\mathrm{Re}_d = 2.14 \times 10^4$. Furthermore, Cheng et al. (2003) studied the performance of LES and RANS over an array of cubes at $\mathrm{Re}_d = 4 \times 10^4$. In addition, a wealth of assessments exist on the study of flow around rectangular buildings (Tominaga, 2015; Blocken, 2018; Zheng et al., 2020; Vita et al., 2020; Hassan et al., 2022) which clarified the limitations of RANS simulations for predicting the flow over rectangular buildings.

In summary, these comparative studies showed that RANS ($k-\omega$ SST) model underestimated the mean and turbulent flow variables, as well as the global flow variables such as drag coefficient (C_d), and the frontal separation length (X_F). It also overestimated the turbulent kinetic energy (TKE) at the stagnation region in front of the cube. Further, $k-\omega$ SST model is unable to predict the flow separation at the top surface of the cylinder and significantly overestimated the length of the recirculation region (X_R) at the near-wake. The overestimation of the recirculation region was attributed to the reduced momentum exchange in the wake due to vortex shedding from cylinder side surfaces (Rodi, 1997). Thus, it becomes important to analyze and correct the performance of the RANS models in predicting the flow around wall-mounted cylinders.

The restrictions of the RANS models motivated researchers to consider RANS formulation and approximation modifying or correcting their results. The RANS eddy-viscosity hypothesis contains several constant coefficients that differ between models. Coefficients are calculated using a combination of experimental observations and dimensional analysis, typically in a simplified ar-

rangement (Hoffman, 1975; Jones and Launder, 1973). Adjusting the coefficients is one of the approaches to improve RANS model prediction that was proposed in several studies on bluff bodies (Shimada and Ishihara, 2002; Mohamed and Wood, 2017; Liu et al., 2017). Development of the turbulence model is a different strategy, which emphasizes innovative ways to improve turbulence models by addressing the closure modeling and the glaring shortcomings of the eddy-viscosity hypothesis (Schmitt, 2007). Mohamed and Wood (2017) presented a modified RANS turbulence model only for enhanced Turbulence Kinetic Energy (TKE) and stagnation prediction over rectangular buildings. The mentioned approaches for modifying the RANS formulation are characterized by case-depended limitations and they are bounded by specific flow behavior.

2.4 Machine Learning (ML)

Machine learning techniques have been utilized in fluid mechanics since the 1940s (Kolmogorov, 1941). In recent studies of fluid mechanics, the demand for using different machine learning algorithms is increased because of the accessibility to huge amounts of data. In this study, machine learning is utilized for correcting the RANS $k-\omega$ SST simulation in estimating quantitative wake characteristics behind rectangular cylinders.

Efforts to enhance the capabilities of RANS models have recently focused on the development of new turbulence models with constant calibrations, which has increased interest in new machine-learning tools. These techniques can either assist CFD in the analysis of fluid mechanics problems, typically for faster predictions, or supplement CFD simulations to improve their accuracy. Thus, artificial intelligence and data-driven models are popular in multiple and diverse applications due to digitalization and the availability of big data (Calzolari and Liu, 2021). To be more specific, popular machine learning techniques that cost-effectively predict non-linear processes within high-dimensional fields are known as Artificial Neural Networks (ANN). The structure and operation of the human brain nervous system serve as inspiration for artificial neural networks, sometimes referred to as neural networks. Its objective is to investigate the nature of human intelligence via an

examination of the structure and functioning of the brain. Further, the machine becomes artificially intelligent through simulation. Neurons are the fundamental building blocks of neural networks, and by connecting a lot of neurons together, a neural network may produce a variety of intelligent actions. Each neuron has the ability to receive a set of input signals from other neurons, with each input having a corresponding weight. The output of each neuron is determined by the weighted sum of all input signals.

There are several techniques to link neurons in neural networks. Different connecting techniques result in various network connection models (Huang et al., 2020). In a feedforward network also known as forward propagation, the input layer, middle layer, and output layer of the neurons are organized in a hierarchy. Only the input from the layer before is accepted by each layer of neurons. The layer has linked networks that allow the neurons to communicate with one another in addition to taking information from the previous layer. Back propagation algorithm (Rumelhart et al., 1986) involves returning the output error in a certain order, layer by layer, and modifying the connection weight of each layer of neurons in accordance with the returned error. In Figure 2.3 the architecture of the backpropagation Multi-Layer Perceptron (MLP) neural network can be seen, which includes for example 5 layers with 3 hidden layers, 3 inputs nodes, and 2 output nodes or units.

Recent investigations utilized neural networks in fluid mechanics, particularly in CFD simulations, to correct existing models by adjusting eddy viscosity constants (Huijing et al., 2021; Yarlanki et al., 2012; Luo et al., 2020), or to develop new turbulence model (Ling et al., 2016; Singh et al., 2017; Geneva and Zabaras, 2019; Zhao et al., 2020). Yarlanki et al. (2012), for example, optimized the model constants of $k - \epsilon$ turbulence model for the temperature in a data centre of an air conditioning unit, using an MLP neural network by comparing simulated data with experimentally obtained temperature values, resulting in a 35% reduction in absolute average error. Furthermore, using a deep learning MLP neural network, Geneva and Zabaras (2019) proposed several modifications of the $k - \epsilon$ model by high-fidelity LES simulation for prediction of the flow on two geometries at different Reynolds numbers: the backwards step and wall-mounted cube.

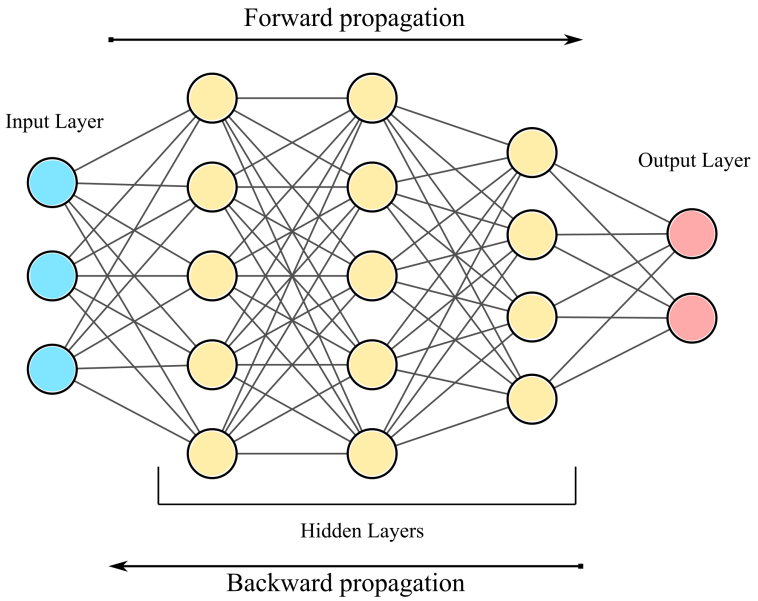

Figure 2.3: The structure of a 5-layer MLP neural network.

By looking at these studies, however, application of the artificial neural network model accelerated the computational work and reduced the computational cost. Case sensitivity and inherent complexity of the fluid flow governing equations demand more research to reach satisfying outcomes compared to the high-fidelity case results. While improving turbulence model coefficients using machine learning is still helpful, these algorithms can accomplish considerably more when working with the enhancement of post-processing data. The process involves creating an artificial neural network to increase the accuracy of outcomes from low-accuracy simulations. For example, accuracy of the RANS simulation results is improved by more accurate results, i.e., LES. Sang et al. (2021) proposed an ANN algorithm to improve the RANS prediction of wind (aerodynamic) loads on rectangular buildings with different sizes. This approach decreases the complexity of algorithm training while also offering benefits, including improved accuracy, computational speed, and affordability (Hanna et al., 2020). However, the utilization of MLP neural network on the post-processed results of low accuracy simulations has received lower consideration in earlier literature.

Chapter 3

METHODOLOGY

The performance of the RANS $k-\omega$ SST model in simulating the wake of a wall-mounted rectangular cylinder is initially examined compared to LES. To train a machine learning algorithm for the correcting RANS results, a vast amount of data is required along with several variables. To this effect, the flow over various sizes of rectangular wall-mounted cylinders with a range of heights and depths is examined in this study. The width (d) of the cylinder is used to normalize all cylinder dimensions, such that aspect ratio (AR) is defined by h/d (where h =height) and depth ratio (DR) is l/d (where l =length), shown in Figure 3.1. 49 cylinders are considered with aspect ratio and depth ratio ranging from 1 to 4 at 0.5 increments. This results in the experimentation matrix of 7 by 7 size based on cylinder heights and depths. The cases are selected based on their usage for engineering applications in the industry and urban structures. In addition, the Reynolds number is $\mathrm{R}e_d = \frac{dU_0}{\nu} = 2.5 \times 10^3$, which guarantee that the flow regime is turbulent (Zhang, 2017; Zargar et al., 2022). Large Eddy Simulation results are used to train the neural network algorithm for correcting RANS results in modeling the wake of cylinders. The incompressible, isothermal flow field is numerically solved using RANS based $k-\omega$ SST turbulence model (Menter, 1994), and Dynamic Smagorinsky LES (Davidson, 2020). All simulations are completed in OpenFOAM, an open-source, finite-volume-based computational fluid dynamics toolbox (Weller et al., 1998; OpenCFD, 2019). The multi-layer perceptron backpropagation artificial neural network with dif-

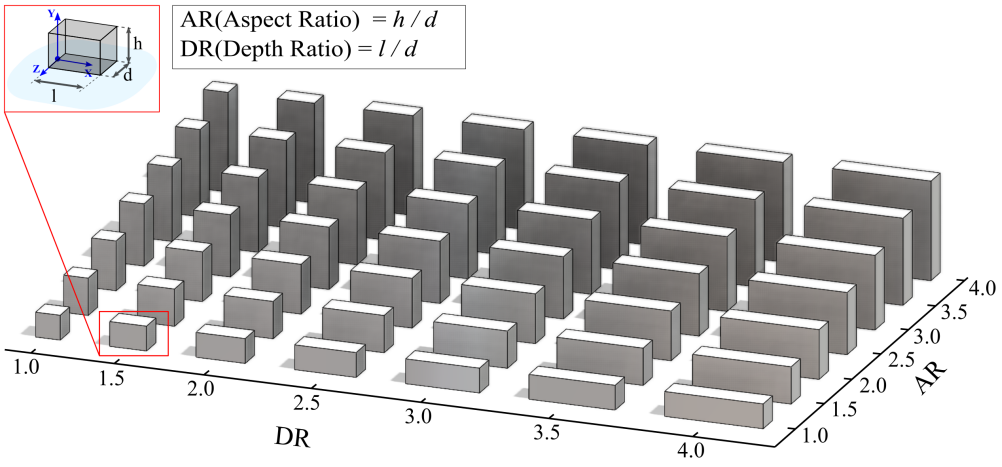

Figure 3.1: (Top) Comparison map of cylinder sizes, varying with both aspect-ratio and depth-ratio; (Bottom) Schematics of the wall-mounted cylinder.

ferent functions is employed as a machine learning algorithm to correct $k-\omega$ SST model results for the near-wake of the rectangular cylinder.

3.1 Numerical simulations

Schematic of the computational domain is shown in Figure 3.2. The streamwise, normal and spanwise directions are represented by x, y and z respectively. The computational domain has an upstream length of $L_U = 10d$, downstream length of $L_d = 20d$, width of $W = 12d$ and height of $H = 7d + h$. A non-homogeneous, multi-block grid consisting of $10\times10^6 - 40\times10^6$ hexahedral elements were utilized for both RANS and LES simulations. As an example, the grid for the case of a cylinder with an aspect ratio of 2 and depth ratio of 2 is shown in Figure 3.3. The grid was designed similarly to past studies (Goswami and Hemmati, 2022; Zargar et al., 2021), such that the finest elements were placed near the cylinder and the walls. This enabled accurate simulations of major wake phenomena, such as the recirculation zone and shear layers that are dominated by large velocity and pressure gradients. Furthermore, the expansion ratio of the grid was kept below 3% to ensure smoothness. A constant uniform velocity inlet boundary condition was used at the inlet, while a Neumann-type (zero normal gradient) outflow boundary condition was set at the

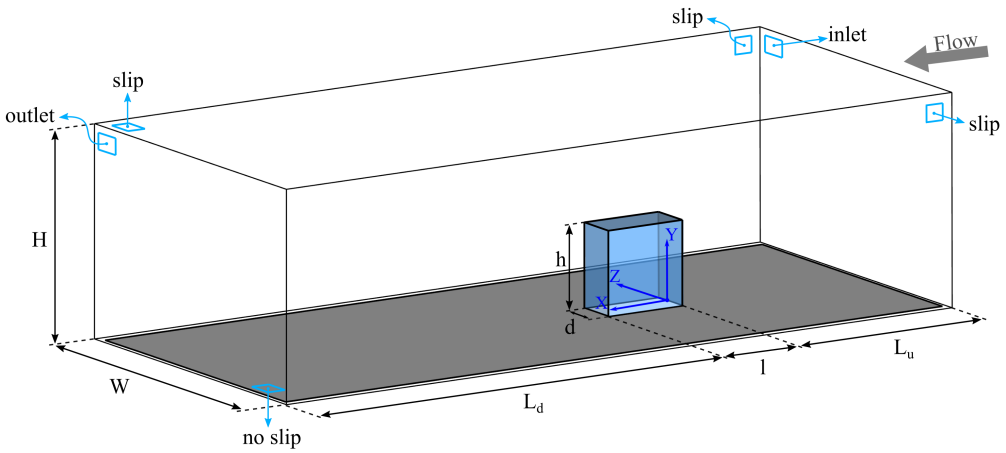

Figure 3.2: Schematic of the computational domain (Not to scale).

outlet boundary based on $\frac{\partial \phi}{\partial x_i} = 0$, where ϕ is any flow variable. The ceiling and lateral sides were modelled as free-slip impermeable boundaries, which enables zero normal velocity and zero shear stress for viscous flow. A no-slip wall boundary condition was used for the cylinder surfaces and the ground.

In the present study, RANS based $k - \omega$ SST (Menter, 1994) turbulence model is used to model the flow around wall-mounted cylinders. The governing RANS equations and details of the turbulence model are provided in Section 2.3.2. This model selection follows the recommendation of Zhang (2017), who evaluated the flow over a finite circular cylinder at $\mathrm{Re}_d = 2 \times 10^4$ using eight RANS-based turbulence models, including $k - \omega$ SST, $k - \omega$, Realizable $k - \epsilon$, RNG $k - \epsilon$, RSA $k - \epsilon$, and Launder-Sharma Low-Re $k - \epsilon$, along with two sub-grid scales (SGS) models, such as LES. Zhang (2017) concluded that the $k - \omega$ SST model showed consistent performance compared to LES, specifically for global flow quantities such as mean drag coefficient ($\overline{C}_d$) and mean surface-pressure coefficient ($\overline{C}_p$), as well as mean velocity and pressure fields. Further, $k - \omega$ SST model is the combination of the standard $k - \omega$(Wilcox, 2006) and $k - \epsilon$ model (Jones and Launder, 1972) and has shown better performance in terms of predictability of flow features in regions of negative pressure gradient (Moukalled et al., 2015). All discretized equations were solved using *simpleFoam*, a steady-state solver for incompressible, turbulent flows incorporating the Semi-Implicit Method for Pressure-Linked equations (SIMPLE) algorithm. The second-order

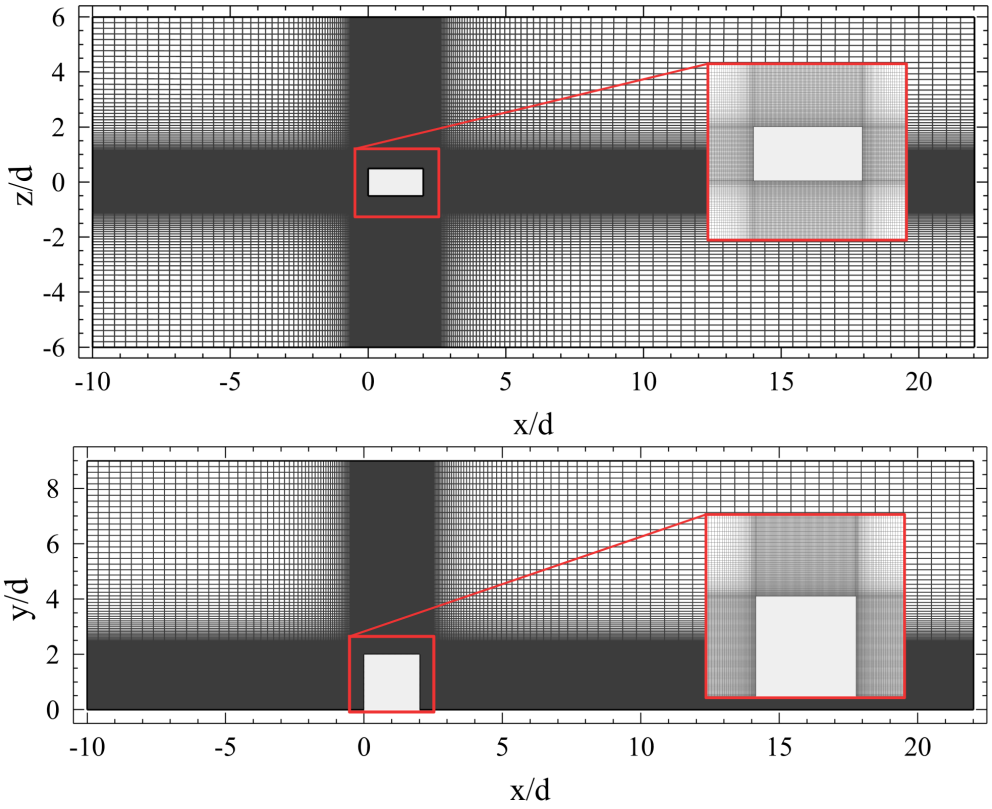

Figure 3.3: The distribution of the grid for the case of cylinder with $AR = 1$ and $DR = 2$ at $z/d = 0$ (bottom) and $y/d = 0.5$ (top).

accurate and bounded numerical discretization schemes were employed for solving the convective and diffusive fluxes. The convergence criterion was set as the root-mean-square of momentum residuals of 10^{-6}. All RANS simulations were completed using 64 Intel Platinum 8160 F Skylake 2.1 GHz cores and 192 GB of shared memory, using an average of 7.5×10^3 core-hours per simulation, on Digital Research Alliance of Canada computing clusters.

Large Eddy Simulation is based on spatially filtered instantaneous Navier-Stokes and continuity equations to discriminate between the large and small-scale structures in the flow. The larger scales are solved directly, while the smaller scales are modelled using the sub-grid scale Leonard stress tensor (Durbin and Reif, 2011):

$$\widehat{\tau}_{ij}^{SGS} = \widehat{u_i u_j} - \widehat{u}_i \widehat{u}_j = -\nu_{SGS} \left(\frac{\partial \widehat{u}_j}{\partial x_i} + \frac{\partial \widehat{u}_i}{\partial x_j} \right) \tag{3.1}$$

The Dynamic Smagorinsky method (Durbin and Reif, 2011) is employed to calculate the SGS stress tensor using the eddy viscosity approach as follows:

$$\widehat{\tau}_{ij}^{SGS} = -2\nu_{SGS}\widehat{S_{ij}}, \tag{3.2}$$

where $\widehat{S_{ij}}$ is the rate of the stress tensor. More details on LES Dynamic Smagorinsky formulation were provided in Section 2.3.1. The filtered momentum and continuity equations were solved using the *pimpleFoam* solver, which employs the PIMPLE algorithm, which is a combination of Pressure Implicit with Splitting Operators (PISO) and SIMPLE algorithm, for coupling of the pressure and velocity fields. The spatial and temporal discretizations are second-order accurate and implicit backward Euler schemes, respectively. The residual root-mean-square of 10^{-6} was set as the criteria for convergence for each time step. The time marching simulations were carried out by selecting a time step of $\Delta t^* = \Delta t U_0/d = 0.003$. The maximum Courant-Friedrichs-Levy number for these simulations was 0.4. All LES simulations were continued for 20 flow-through times, where a flow-through time is the time that the fluid takes to travel between inlet and outlet. The data for the last 10 flow-through times were considered for post-processing. All LES simulations were completed using 96 Intel Platinum 8160 F Skylake 2.1 GHz cores and 192 GB of shared memory, using an average of 3×10^4 core-hours per simulation, on Digital Research Alliance of Canada computing clusters.

3.1.1 Verification and Validation

Numerical simulations were verified by evaluating their sensitivity to grid resolution and domain sizes, following the recommendation of Hemmati et al. (2018). To address the former, the computational domain was designed larger than the previous studies (Yakhot et al., 2006; Krajnović, 2011; Saha, 2013; Saeedi et al., 2014; Zargar et al., 2021; Goswami and Hemmati, 2022). Furthermore, the current domain size was designed identical to that of Zargar et al. (2021) and Goswami and Hemmati (2022), who provided an extensive sensitivity study. Sohankar et al. (1998) and

Cases	$\overline{C}_d$	$\lvert\Delta\overline{C}_d\rvert$ %	$\overline{C}_l$	$\lvert\Delta\overline{C}_l\rvert$ %	N_{total}	y^+_{max}
Grid 1	1.34	_	0.266	_	5.1×10^6	3.1
Grid 2	1.30	2.98	0.271	1.88	15.1×10^6	1.5
Grid 3	1.27	2.3	0.281	3.69	19.6×10^6	0.8
Grid 4	1.27	0.08	0.281	0.05	23.2×10^6	0.44

Table 3.1: Comparison of mean drag ($\overline{C}_d$) and lift coefficients ($\overline{C}_l$) for all the grids.

Saha (2013) provided a criteria for blockage ratio (β) and the domain height (H), such that $\beta = (d \times h)/(W \times H) \leq 0.05$ and $H \geq h + 5d$, to ensure negligible effects on the global flow variables. For the current study, these were set at $\beta \leq 0.04$ and $H \geq 7d$.

The grid sensitivity analysis was carried out for the LES simulations using four successively refined grids for the case of flow around a cylinder with an aspect ratio and depth ratio of 2: Grid 1 (5.1×10^6), Grid 2 (15.1×10^6), Grid 3 (19.6×10^6), and Grid 4 (23.2×10^6). The cylinder geometry was selected for the grid sensitivity since it is expected to provide the most complex unsteady wake dynamics compared to low aspect-ratio cylinders (Zhang, 2017; Rastan et al., 2021). Table 3.1 shows a comparison of the mean drag ($\overline{C}_d$) and lift coefficients ($\overline{C}_l$) for all cases. The results in Table 3.1 show that the differences in Grid 3 and Grid 4 are not significant for all global (integral) variables. As such, we further compare the profiles of mean streamwise velocity ($\overline{u_x}/U_0$) at mid-plane ($z/d = 0$) and various axial locations, $x/d = 3, 5$ and 7. For brevity, only the result at $x/d = 3$ is presented in Figure 3.4, which shows the maximum discrepancy of less than 1% between Grid 3 and Grid 4. Hence, it is reasonable to conclude that Grid 3 was sufficient to capture the global and mean flow features.

Examination of the spatial resolution was complemented by calculating the ratio of grid size to Kolmogorov length scale, given by $\Delta/\eta = \frac{(\Delta x \times \Delta y \times \Delta z)^{\frac{1}{3}}}{[\frac{\nu^3}{\epsilon}]^{\frac{1}{4}}}$, where ϵ is the dissipation rate and derived from the gradient of the fluctuating velocity. Previous studies (Rastan et al., 2021; Goswami and Hemmati, 2022; Zargar et al., 2022) have used a similar method to estimate the grid resolutions for DNS and LES. The later, the value of $\Delta/\eta \leq 40$ is suggested (Celik et al., 2009; Rastan et al.,

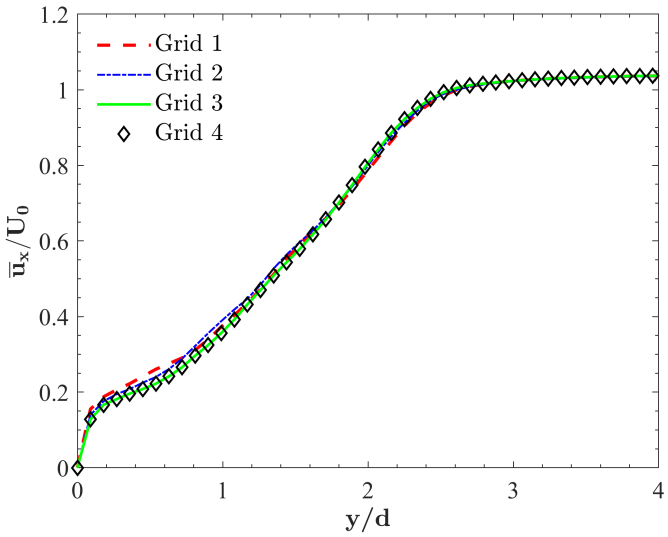

Figure 3.4: Comparison of Time-averaged (mean) streamwise velocity ($\overline{u_x}/U_0$) at $x/d = 3$ and $z/d = 0$ for all grids.

2021). Further, Yakhot et al. (2006) suggested a criterion of $2 \leq \Delta/\eta \leq 5$ in the immediate vicinity of a wall-mounted cylinder. Figure 3.5 presents the results of Δ/η for the cylinder with aspect-ratio and depth-ratio of 2 and 4, at the plane in the middle height of the body. The results show that Δ/η is less than 10 for the entire domain, with $\Delta/\eta \leq 5$ in the immediate vicinity of the cylinder. Further, Δ/η increases with x/d so that the maximum value of Δ/η at $x/d \approx 5$ increases to $\Delta/\eta = 10$ from 5 at $x/d \approx 15$. Larger values of Δ/η denote that the turbulence levels intensify in the wake, and subsequently larger dissipation rate and smaller Kolmogorov length scales appear. These results further provide confidence that the numerical setup and grid resolution are sufficient to capture the flow around wall-mounted cylinders accurately.

For validation, to the best knowledge of the author, there are no studies in literature on the wake of wall-mounted cylinders at this particular Reynolds number (2.5×10^3) and parameter space. Thus, a square cylinder with an aspect ratio of 4 was numerically analyzed using LES at $\mathrm{Re}_d = 1.2 \times 10^4$ for validation purposes. The results were compared with the experiments Saeedi et al. (2014). Figure 3.6a shows this comparison for mean streamwise velocity ($\overline{u_x}/U_0$) at $y/d = 1$ and $z/d = 0$. The results indicate a discrepancy of $\sim 6\%$ between LES and experiments, while RANS models overestimated the velocity deficit. Further validation of the RANS simulation

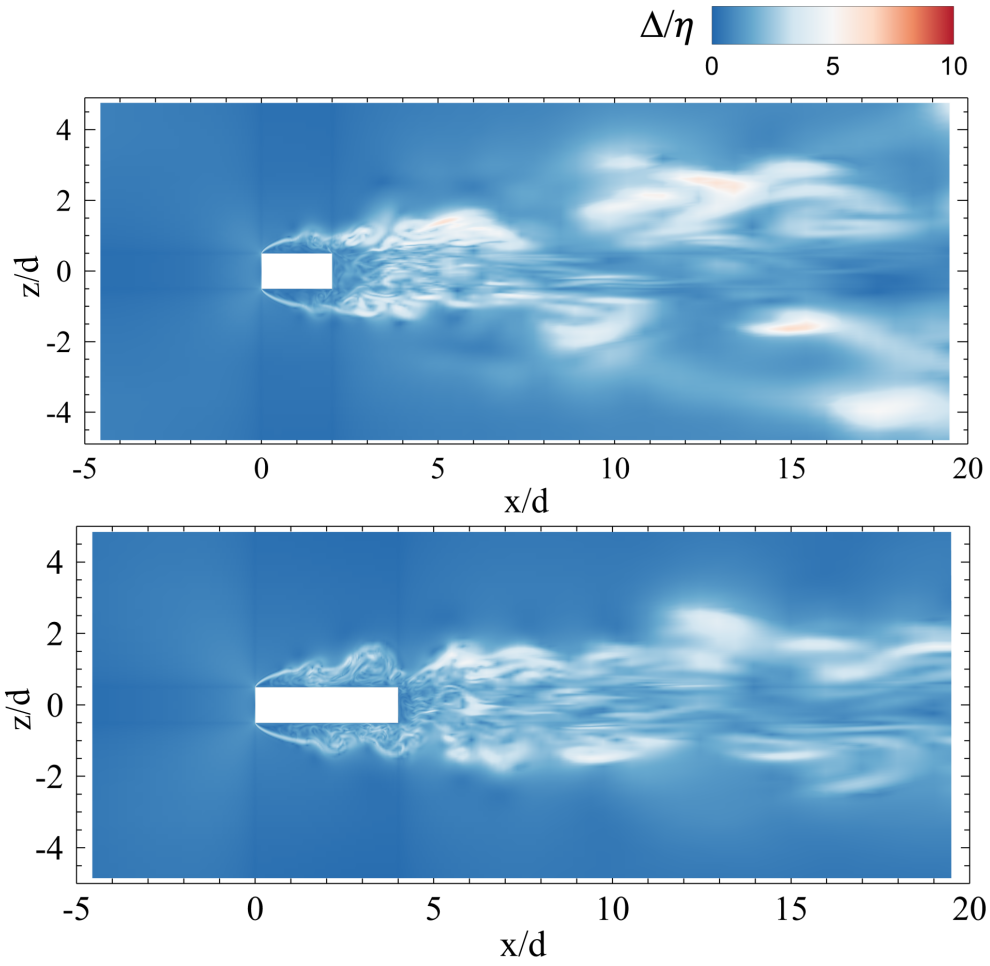

Figure 3.5: The ratio of spatial grid size to the Kolmogorov length scale (Δ/η) for the intermediate case (AR = DR =2) (top) and the largest case (AR = DR = 4) (bottom) at the cylinder mid-height plane.

was performed by comparing the upstream velocity profile with that of analytically calculated Blasius laminar boundary solution. The results of this comparison are shown in Figure 3.6b, which indicates that the RANS model captures the incoming boundary layer with reasonable accuracy. Hence, the extensive verification and validation study provides us with sufficient confidence in the accuracy of results obtained using RANS and LES.

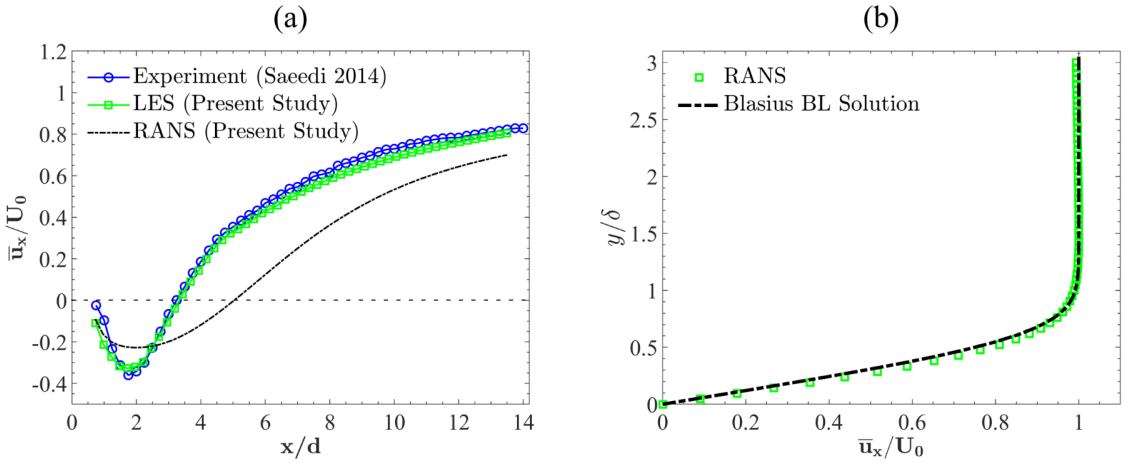

Figure 3.6: (a) Comparison of mean streamwise velocity ($\overline{u_x}/U_0$) obtained from LES and RANS with experimental results of Saeedi et al. (2014); (b) Blasius boundary layer profile compared with boundary layer profile at upstream region before the cylinder.

3.1.2 Artificial Neural Network

The machine learning algorithm used in this study is a multi-layer perceptron backpropagation artificial neural network, also known as a neural network. This algorithm is utilized to correct RANS $k-\omega$ SST model results. The model and the architecture of the neural network algorithm are provided below.

Model of the neural network

The model of the algorithm and training procedures were inspired by multiple studies in literature (Bonaccorso, 2018; Ng, 2020; Bonaccorso, 2020; Brunton et al., 2020; Calzolari and Liu, 2021). The supervised learning algorithm in the regression model was selected because the data set is given and it is already known what the correct output should resemble. Thus, it is established that there is a relationship between the input X and the output Y (Equation 3.3). Moreover, the aim is to predict results within a continuous output, which means that input variables are being mapped to a continuous function:

$$Y = f(X), \tag{3.3}$$

According to the size of the data set, the time-independent training system, and the fact that no feedback is required from previous data, the appropriate algorithm for this study is the back-propagation neural network. The method is selected amongst all machine learning algorithms for supervised learning with the non-linear regression function, including Support Vector Machine (SVM), Extreme Learning Machine (ELM), and BP neural network (Huang et al., 2020) or deep-learning algorithms, like Convolutional Neural Networks (CNN), and Long-Short-Term-Memory Recurrent Neural Network (LSTM-RNN) (Hochreiter and Schmidhuber, 1997; Goodfellow et al., 2016; Calzolari and Liu, 2021). Moreover, Hintea. et al. (2015) compared different machine learning algorithms, including a standard MLP neural network, linear regression algorithm, and Random Forest algorithm. The algorithms were utilized for predicting the temperature inside a car. A simpler linear regression model eventually delivered the fastest prediction, while the MLP achieved the highest overall accuracy.

The first layer of the network, known as the input layer (x), goes through hidden layers, and finally structures the output layer that would be the hypothesis function $h_\theta(x)$ for the algorithm. Each layer has some nodes and the intermediate hidden layers between the input and output layers consist of activation nodes inside their nodes $a_i^{(l)}$, where l represents the layer number and i is the node or unit number. Equation 3.4 shows the general activation function, which contains linear relation of the weights (θ_{ji}^l) and bias (b_i^l), where j is an index belongs to the previous layer ($l-1$) in the layer l. So, each layer is given a separate weights matrix:

$$a_i^{(l)} = g(\sum_j \theta_{ji}^l x_{ji}^l + b_i^l) \tag{3.4}$$

The accuracy of the network is evaluated by the cost function ($J(\theta)$), which calculates the average difference of the hypothesis for each layer with respect to the actual output y. Here the actual outputs are LES simulation outputs. This is done during the implementation of the forward propagation. Equation 3.5 shows $J(\theta)$, where K is the number of output units, and m is the total number of training set data.

$$J(\theta) = \frac{1}{2m} \sum_{i=1}^{m} \sum_{k=1}^{K} \left[\left(h_\theta \left(x^{(i)} \right)_k - y_k^{(i)} \right)^2 \right] + \underbrace{\lambda \sum_{l=1}^{L-1} \sum_{i=1}^{U_l} \sum_{j=1}^{U_{l+1}} \left(\theta_{j,i}^{(l)} \right)^2}_{Regularization} \tag{3.5}$$

The nature of the hypothesis function (h) maps poorly to the trend of the data when there is underfitting, often known as high bias. Usually, it results from a function that is too basic or makes insufficient use of features. On the other hand, a hypothesis function that fits the existing data but does not generalize well to forecast new data results in overfitting, or high variance. It frequently results from a complex function that adds extra curves and angles that have nothing to do with the data. To overcome this problem, after the square brackets in Equation 3.5, the regularization function is added to the cost function to perform the best fitting for the data. In Equation 3.5 U_l is the number of units in layer l (not counting the bias unit), L is the total number of layers, and the regularisation parameter λ controls how much our θ parameters' costs are inflated.

The neural network optimization technique (backpropagation) minimizes $J(\theta)$, and it is comparable to gradient descent in a basic linear regression model. Loss function of a minimization algorithm additionally computes derivatives with respect to the weights and bias at each node and layer through back-propagation and updates them and will track the difference between the prediction and the real value (Calzolari and Liu, 2021). The goal is to determine the global minimum of the cost function, but the approach discussed primarily determines the local minimum based on the initialization of the learning network. To find a global minimum, another optimization method is utilized, namely backpropagation learning based on the Levenberg-Marquardt Algorithm (LMA). The Gauss-Newton algorithm (GNA) and the gradient descent technique are interpolated by the LMA. Because the LMA is more resilient than the GNA, it frequently finds a solution even when it starts far from the ultimate minimum (Ranganathan, 2004; Sapna et al., 2012).

Training of the neural network algorithm can be accelerated by keeping all of the input values inside a narrow range. This is due to the fact that when the variables are highly unequal, the algorithm will oscillate inefficiently down to the optimum since the variables will decline quickly on small ranges and slowly on wide ranges. To do so, the feature scaling function is represented

in Equation 3.6, where s_i is the standard deviation, and μ_i is the average of all the input variable values for feature (i). The feature scaling function can keep all the data in a similar range ($i.e.$, between 0 and 1):

$$x_i = \frac{x_i - \mu_i}{s_i} \tag{3.6}$$

With neural networks, initializing all theta weights to 0 does not work. All nodes will repeatedly update to the same value when it backpropagates. As an alternative, the weights can be initialized for the θ matrices at random between for example ϵ and $-\epsilon$.

The flowchart in Figure 3.7 represents how the ANN works and the algorithm learning trajectory. In this flowchart, data set input includes aspect ratio, depth ratio, RANS data, and LES data as the actual data. Training of the network begins with the feature scaling and after random initialization. The feedforward function is applied to the neural network to calculate the values for weights in the neurons. Then, the cost function evaluates the weights in each unit of the hidden layers. Afterwards, the backpropagation and optimization functions began to effectively find the minimum of the cost function and update the weights from the last layer to the first in each iteration. The hypothesis function or the trained algorithm contains the optimum weights for predicting data when the iteration of the optimization stops at a certain order of error.

Neural network training and validation

The architecture of the neural network is shown in Figure 3.8a. Five layers make up the neural network, including an input layer, an output layer, and three hidden layers. There are 8 input units including AR, DR, X_R, X_F, X_T, $\overline{C}_d$, $\overline{C}_l$, and $\overline{C}_{bp}$. Moreover, as can be seen in Figure 3.8a, the output layer has 6 hypothesis functions for prediction. There are 8 activation units plus one bias unit that construct 9 neurons for each hidden layer. The decision for the optimum number of neurons and the hidden layers was made based on the mean squared error, which was calculated for different numbers of neurons and layers in a constant initialization to evaluate the least error

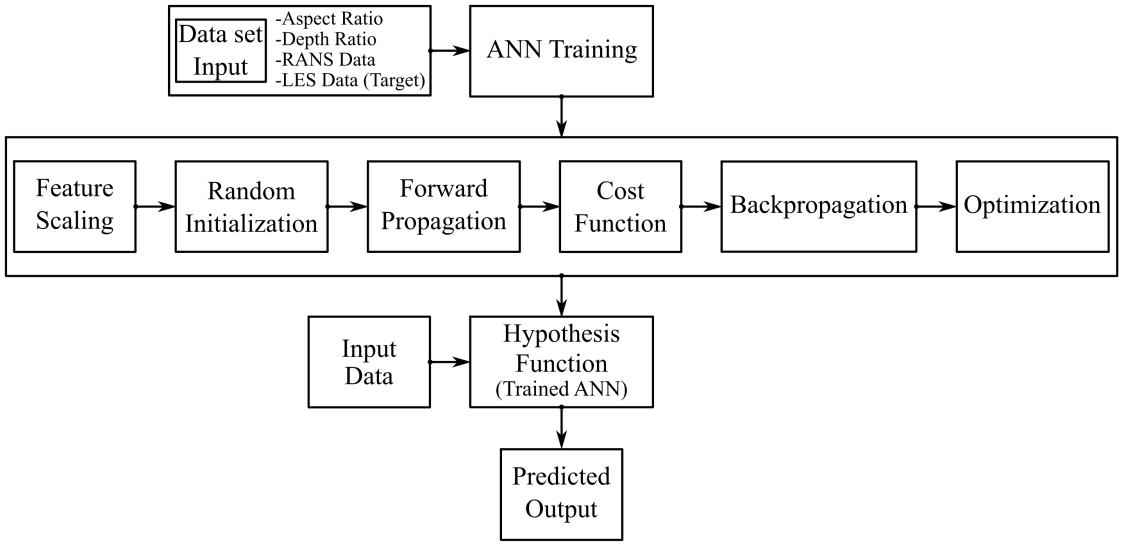

Figure 3.7: Flowchart for the artificial neural network training process.

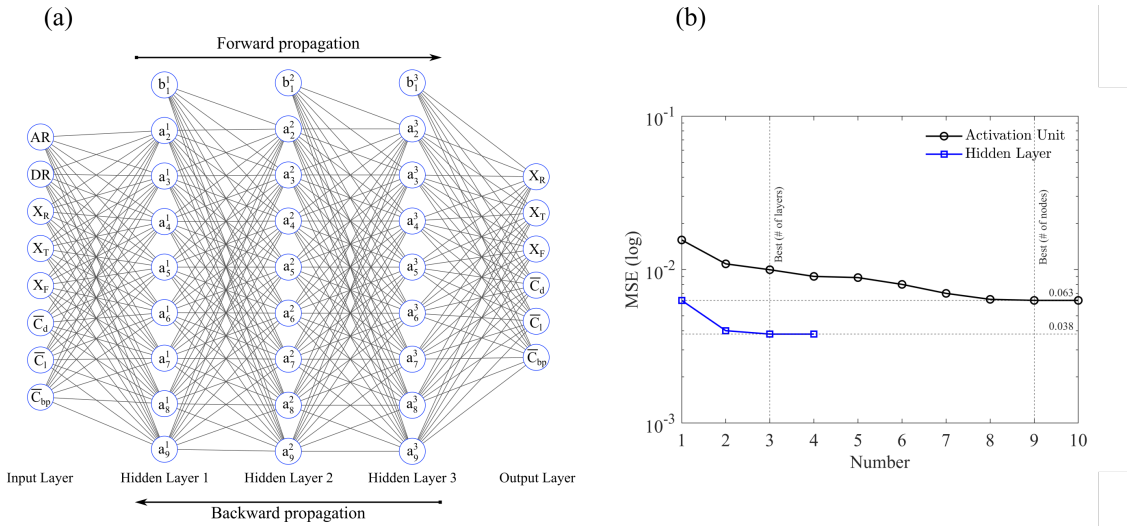

Figure 3.8: (a) The schematic of the neural network architecture. (b) Prediction error of each neural network data set.

(Figure 3.8b). It is concluded that the optimum number of activation units and hidden layers in terms of training time and accuracy is 9 and 3, respectively.

To train the algorithm, there are 49 sets of data divided into training, validation, and test sets. Depending on how big the data set is, size ratio of each set varies. The ratios for the training set, validation set, and test set in this study are 70%, 15%, and 15% of the total data set, respectively. The validation data set is used to control the learning process and to find the polynomial degree with

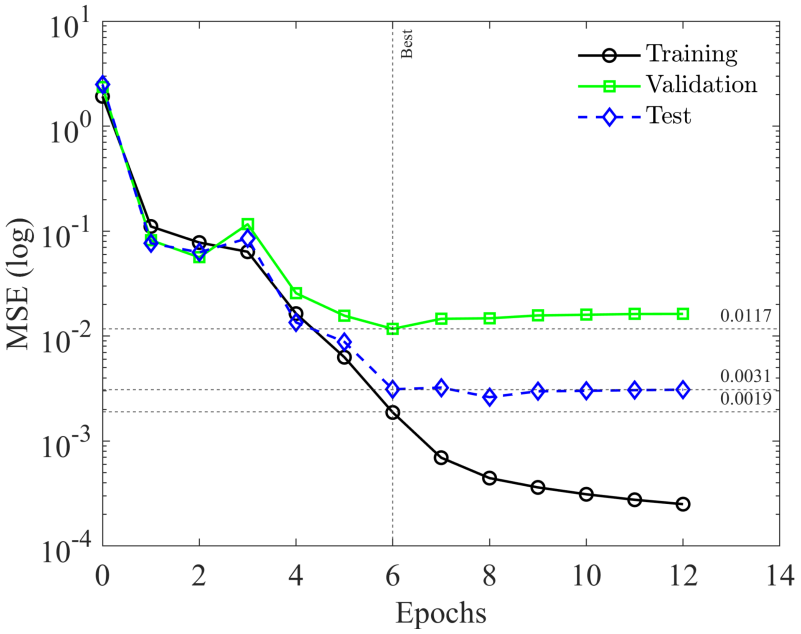

Figure 3.9: Prediction error of each neural network data set (Training data, Validation data, and Test data).

the least error, while the training is modifying the hyperparameters of the algorithm. Additionally, the test set is used for evaluating the generalization error of the ANN for unseen data, since it does not take part in training. Instead, the test set is used exclusively for comparison with the expected value after training to determine the discrepancy between the simulation result and the prediction result. Thus, the measured error of the training set is always lower than the test set. Figure 3.9 represents the mean squared error of the training, validation, and test data set. The plot also confirms that the generalization error is sufficiently low in order to satisfy the precision requirement of the prediction of the algorithm.

Chapter 4

PERFORMANCE OF THE $k-\omega$ SST MODEL

The performance of $k-\omega$ SST, is examined in terms of their prediction of global flow variables, streamlines and wake profiles in flows around wall-mounted rectangular cylinders with varying aspect ratios and depth ratios. The results are compared with LES simulations of the same flows. The main aim of this chapter is to identify the limitations of the $k-\omega$ SST model in predicting the complex flow dynamics behind finite, wall-mounted cylinders that result in large velocity and pressure gradients. A total of 49 cases with aspect-ratios and depth-ratios varying between $1-4$ are studied, out of which results for 9 representative cases are shown in this chapter, in terms of streamlines and iso-surface contours, for brevity. The chosen cases have aspect ratios of $1, 2.5$ and 4, and depth ratios of $1, 2.5$ and 4.

We begin by looking at the time-averaged (mean) wake topology computed by LES. First, we consider the streamlines shown in Figure 4.1, which shows the flow field at spanwise mid-plane, $z/d = 0$. The overall flow features remain common among all cases, $i.e.$ the flow reattachment length behind the cylinder (X_R), recirculation zone on top of the cylinder (X_T), and front recirculation (X_F) due to roll-up of boundary layer forming the horse-shoe vortex (Simpson, 2001). The dependence of X_R with changing aspect-ratio and depth-ratio is clearly noted. Reattachment

length (X_R) reduces with increasing depth-ratio, while it increases with increasing aspect ratio. An increase in depth-ratio leads to an increase in the strength of downwash flow, which results in shrinking the recirculation zone behind the cylinder (Goswami and Hemmati, 2022). Further, an increase in aspect ratio leads to an increase in the dominance of the upwash flow at a particular depth ratio, thus increasing the size of the recirculation zone (Wang and Zhou, 2009).

The recirculation regions in the front (X_F) and top (X_T) of the cylinder are observed for all cases. The front recirculation region relates to the formation of the horse-shoe vortex, while the top recirculation forms due to leading-edge flow separation. No significant variation is observed in X_F with changing aspect-ratio and depth ratio since the size of the horse-shoe vortex in front of the cylinder depends strongly on the thickness of the boundary layer (Hwang and Yang, 2004). On the other hand, X_T grows with increasing depth-ratio. The shear-layer separation at the leading edges of the cylinder relates to the wake structures forming downstream, especially for small depth-ratio cylinders. Increasing the depth ratio leads to an adverse-pressure gradient forming on the top surface of the cylinder, resulting in flow reattachment (Zargar et al., 2021; Goswami and Hemmati, 2022). Figure 4.1 shows the flow reattachment length on the top surface of the cylinder increasing with increasing depth ratio.

Figure 4.2 shows the mean wake computed by $k-\omega$ SST model. The model succeeds in capturing the major features of the flow topology, which are the shear-layer separation and reattachment processes, as well as the formation of the recirculation region behind the cylinder. The flow separation occurs at the upstream edge of the cylinder, and the lateral width (height) of the recirculation zone exceeds the height of the cylinder slightly ($\approx 18\%$). This remains consistent with LES results in Figure 4.1. The lateral width of the recirculation region on top of the cylinder corresponds to the top recirculation length (X_T) on the roof. The $k-\omega$ SST model significantly overestimated the length of the reattachment region downstream (X_R), underestimated the separation length in front of the cylinder (X_F), and poorly estimated the recirculation length on the top surface (X_T). These differences are attributed to the poor prediction of pressure and velocity gradients immediately

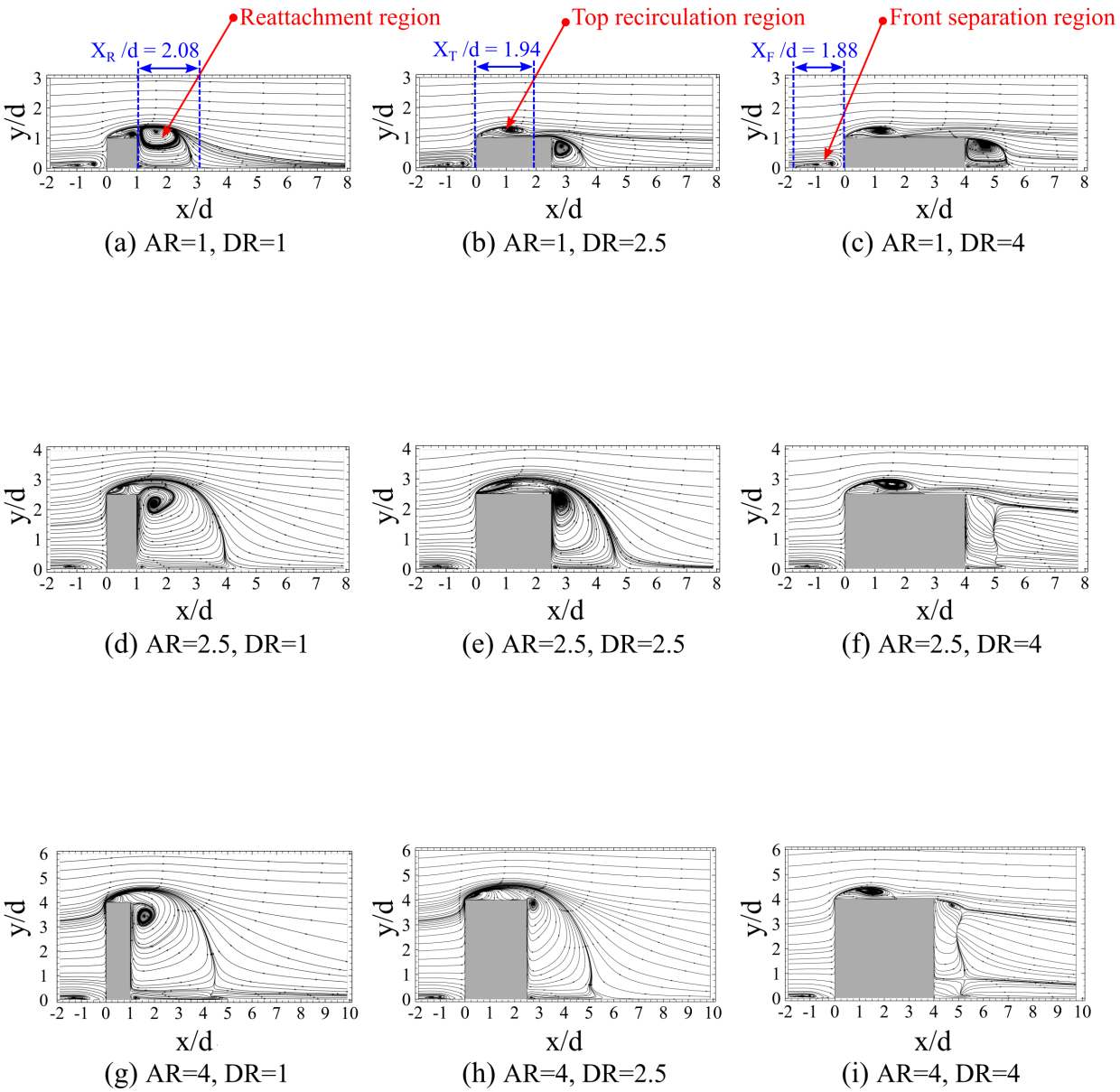

(a) AR=1, DR=1 (b) AR=1, DR=2.5 (c) AR=1, DR=4

(d) AR=2.5, DR=1 (e) AR=2.5, DR=2.5 (f) AR=2.5, DR=4

(g) AR=4, DR=1 (h) AR=4, DR=2.5 (i) AR=4, DR=4

Figure 4.1: Mean velocity streamlines at cylinder spanwise mid-plane, $z/d = 0$, from LES simulations.

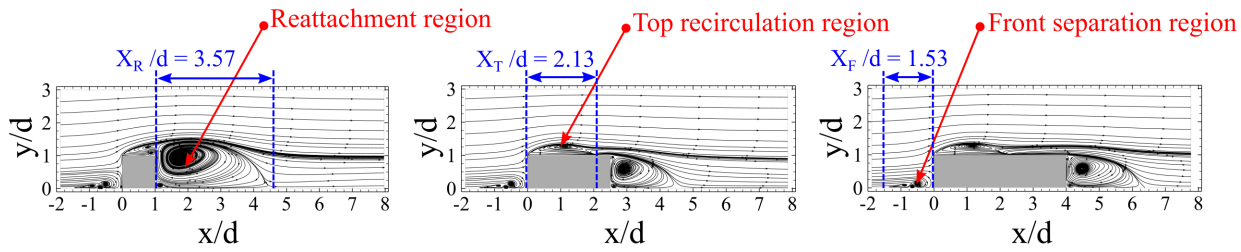

(a) AR=1, DR=1 (b) AR=1, DR=2.5 (c) AR=1, DR=4

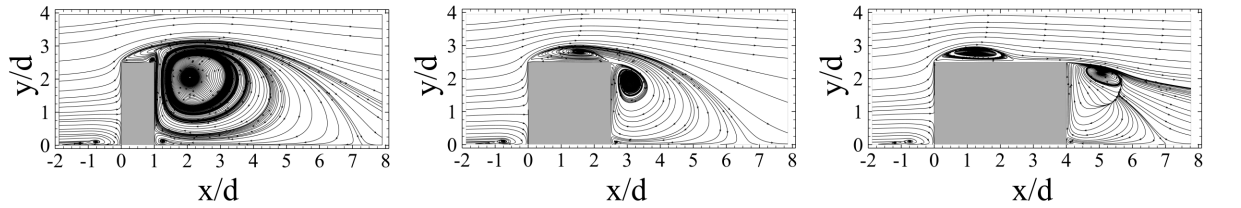

(d) AR=2.5, DR=1 (e) AR=2.5, DR=2.5 (f) AR=2.5, DR=4

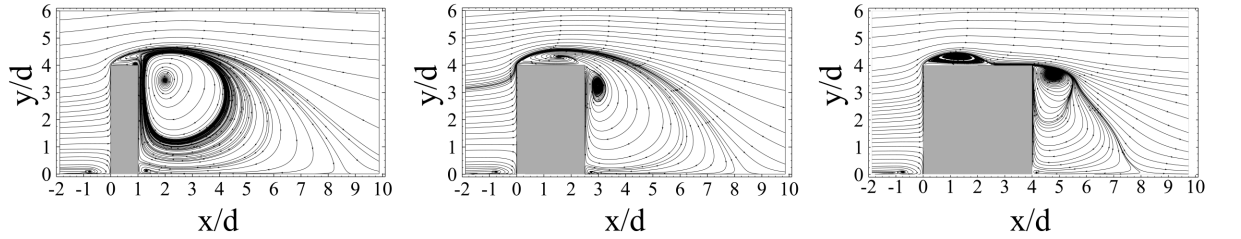

(g) AR=4, DR=1 (h) AR=4, DR=2.5 (i) AR=4, DR=4

Figure 4.2: Mean velocity streamlines at cylinder spanwise mid-plane, $z/d = 0$, from RANS simulations.

downstream of the cylinder. Past studies (Fogaing et al., 2019; Zhang, 2017) have noted a similar discrepancy in flow modelling using RANS.

Further, the experimental work of Dimaczek et al. (1989) on the flow over wall-mounted obstacles revealed a correlation in the prediction of the size of the reattachment region with the flow separation on the leading edge of the obstacle. Accurate estimation of the shear-layer separation at the leading edge results in an accurate prediction of the reattachment region behind the cylinder. In the case of wall-mounted, finite cylinders, the shear-layer dynamics in the vicinity of the cylinder becomes complex due to the various end effects and vortex interactions (Zargar et al., 2022; Goswami and Hemmati, 2022). The consistency of RANS simulations in estimating different reattachment lengths can, thus, be attributed to their inability to capture the leading edge flow separation.

Another important aspect of the mean wake of wall-mounted cylinders is the cross-sectional wake topology. Past studies have reported either dipole or quadruple-type wakes (Wang and Zhou, 2009; Hosseini et al., 2013). The effects of Re, aspect ratio, and boundary layer thickness on transition from one mean wake topology to another have been scrutinized in the past by Rastan et al. (2017, 2021). However, the influence of changing depth ratio remains unexplored to the best of the author's knowledge. Figure 4.3 shows the mean wake topology of wall-mounted cylinders with changing aspect-ratios and depth-ratios by plotting iso-surfaces of the $Q-$criterion coloured by relative mean axial velocity ($\overline{u_x}/U_0$) from LES. Formation of the tip and base vortices, as well as the horseshoe vortex, is indicated for all cases. Increasing the aspect ratio leads to increased intensity of the tip-vortex, which is clearly observed in Figures 4.3a, 4.3d, and 4.3g. The dipole-type cross-sectional wake is also consistent with the past literature (Wang and Zhou, 2009). Increasing the depth ratio leads to shear-layer reattachment on the cylinder surfaces, and subsequently to trailing edge separation (Goswami and Hemmati, 2022). The downwash flow is suppressed with increasing depth-ratio, leading to distortion of the tip-vortex, as observed in Figurse 4.3c, 4.3f, and 4.3i.

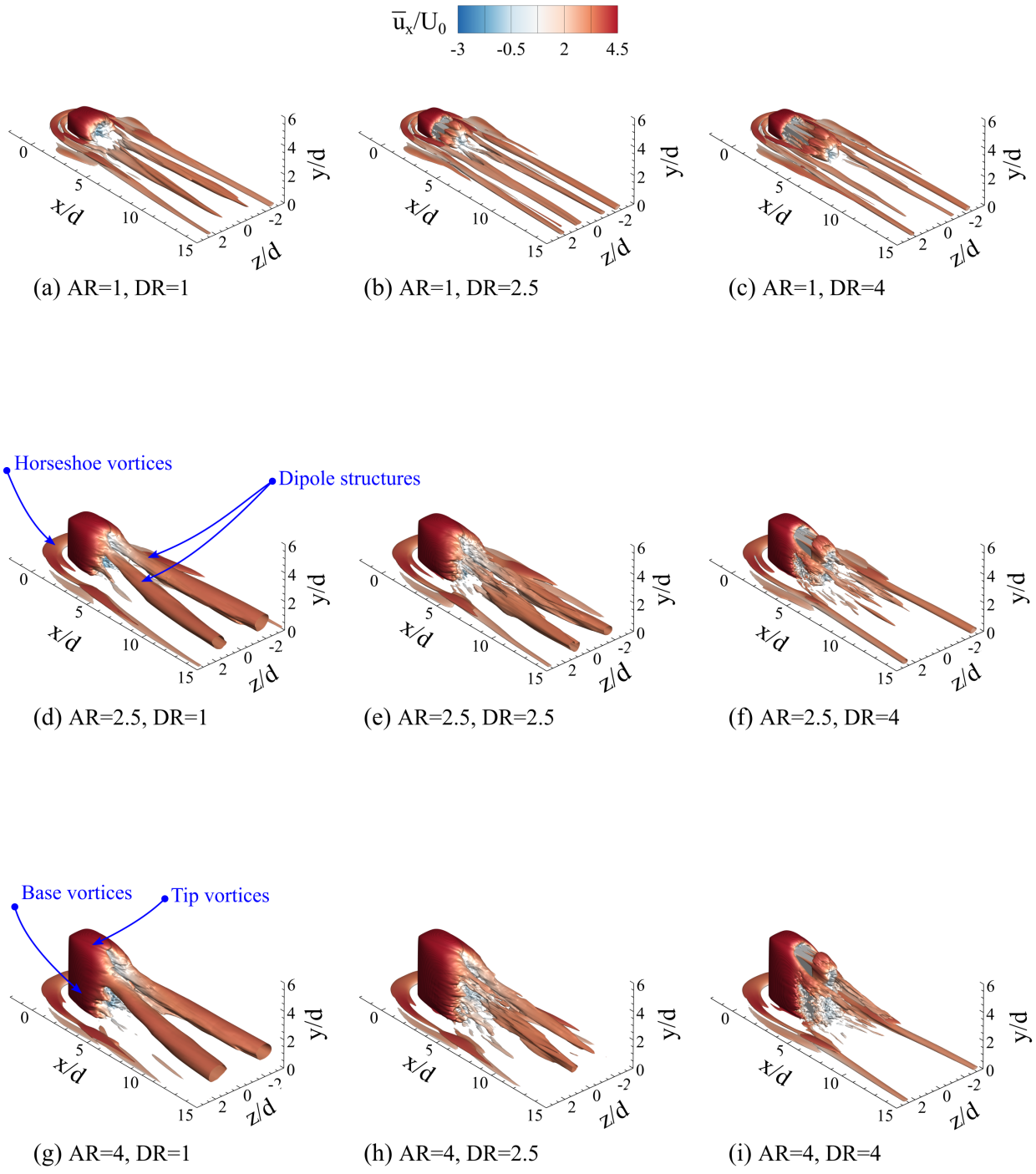

(a) AR=1, DR=1 (b) AR=1, DR=2.5 (c) AR=1, DR=4

(d) AR=2.5, DR=1 (e) AR=2.5, DR=2.5 (f) AR=2.5, DR=4

(g) AR=4, DR=1 (h) AR=4, DR=2.5 (i) AR=4, DR=4

Figure 4.3: Iso-surface of time-averaged wake structure generated using $Q - criterion = 10^{-6}$ colored by relative mean streamline velocity, from LES Simulations.

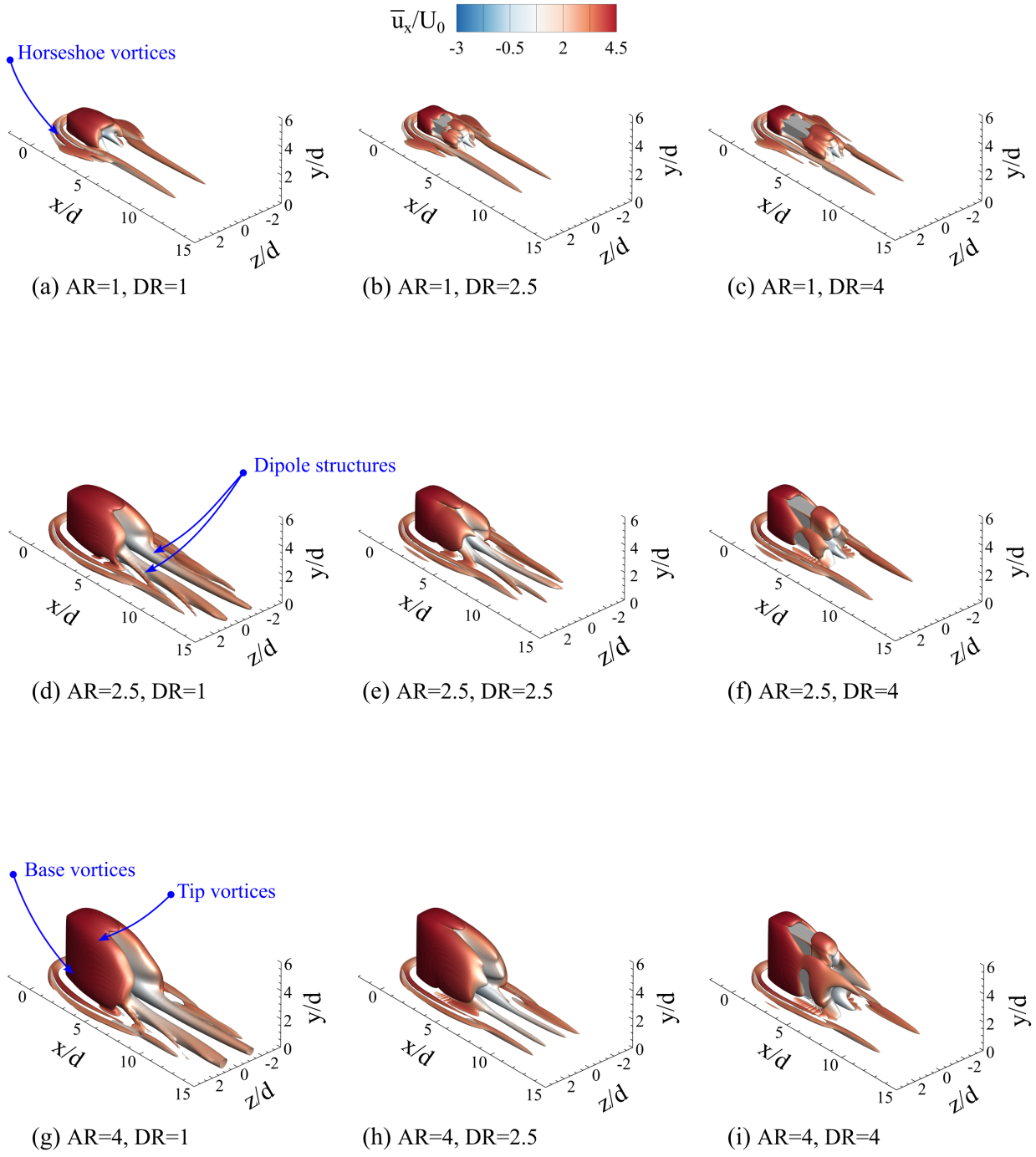

(a) AR=1, DR=1 (b) AR=1, DR=2.5 (c) AR=1, DR=4

(d) AR=2.5, DR=1 (e) AR=2.5, DR=2.5 (f) AR=2.5, DR=4

(g) AR=4, DR=1 (h) AR=4, DR=2.5 (i) AR=4, DR=4

Figure 4.4: Iso-surface of time-averaged wake structure generated using $Q - criterion = 10^{-6}$ colored by relative mean streamline velocity, from RANS Simulations.

Figure 4.4 shows the mean wake topology of wall-mounted cylinders with changing aspect-ratios and depth-ratios by plotting the iso-surfaces of the $Q-$criterion coloured by relative mean axial velocity ($\overline{u_x}/U_0$) from $k-\omega$ SST model. While the model successfully predicts the wake features, such as the tip, base and horseshoe vortices, there are significant discrepancies in the mean wake compared to the LES results in Figure 4.3. The horseshoe and tip vortices, which extend in the downstream wake for LES simulations, disappear behind the cylinder in the case of RANS simulations.

Evolution of the mean wake topology with changing depth-ratio and aspect-ratios is further studied by looking at the mean velocity streamlines at $x/d = 7$, shown in Figures 4.5 and 4.6. The results indicate dipole-type cross-sectional wake topology, which remains unchanged with increasing in aspect ratio and depth ratio. The span of the downstream wake increases with increasing the aspect ratio, while the depth ratio has negligible effect (Goswami and Hemmati, 2022). The formation of dipole-type mean wake topology indicates the dominant influence of tip-vortex or the downwash flow in governing the downstream wake dynamics. Thus, the accurate prediction of tip-vortex in the downstream wake region becomes necessary. The results in Figure 4.6 show discrepancies in the estimation of the dipoles. $k-\omega$ SST model significantly suppresses the tip vortices and horseshoe vortices downstream of the cylinder. Further, for high aspect-ratio cylinders, location of the dipoles remains closer to the ground, contrary to the LES observation in Figure 4.5. Past studies have indicated that the transport of spanwise vortex structures is associated with momentum transport due to stresses and turbulence production (More et al., 2015). Thus, looking at the trends in Reynolds stresses and turbulence kinetic energy production can provide further evidence of the discrepancy.

A quantitative comparison of the reattachment length (X_R), top recirculation length (X_T), and front separation length (X_F) with changing aspect-ratios and depth-ratios is shown in Figure 4.7. The results indicate that $k-\omega$ SST model overestimates X_R while underestimating X_F. The trends in X_R and X_F, however, remain consistent with LES results. Further, the trends in X_T remain consistent with LES for small depth ratios and small aspect-ratio cylinders. Increasing depth-ratio

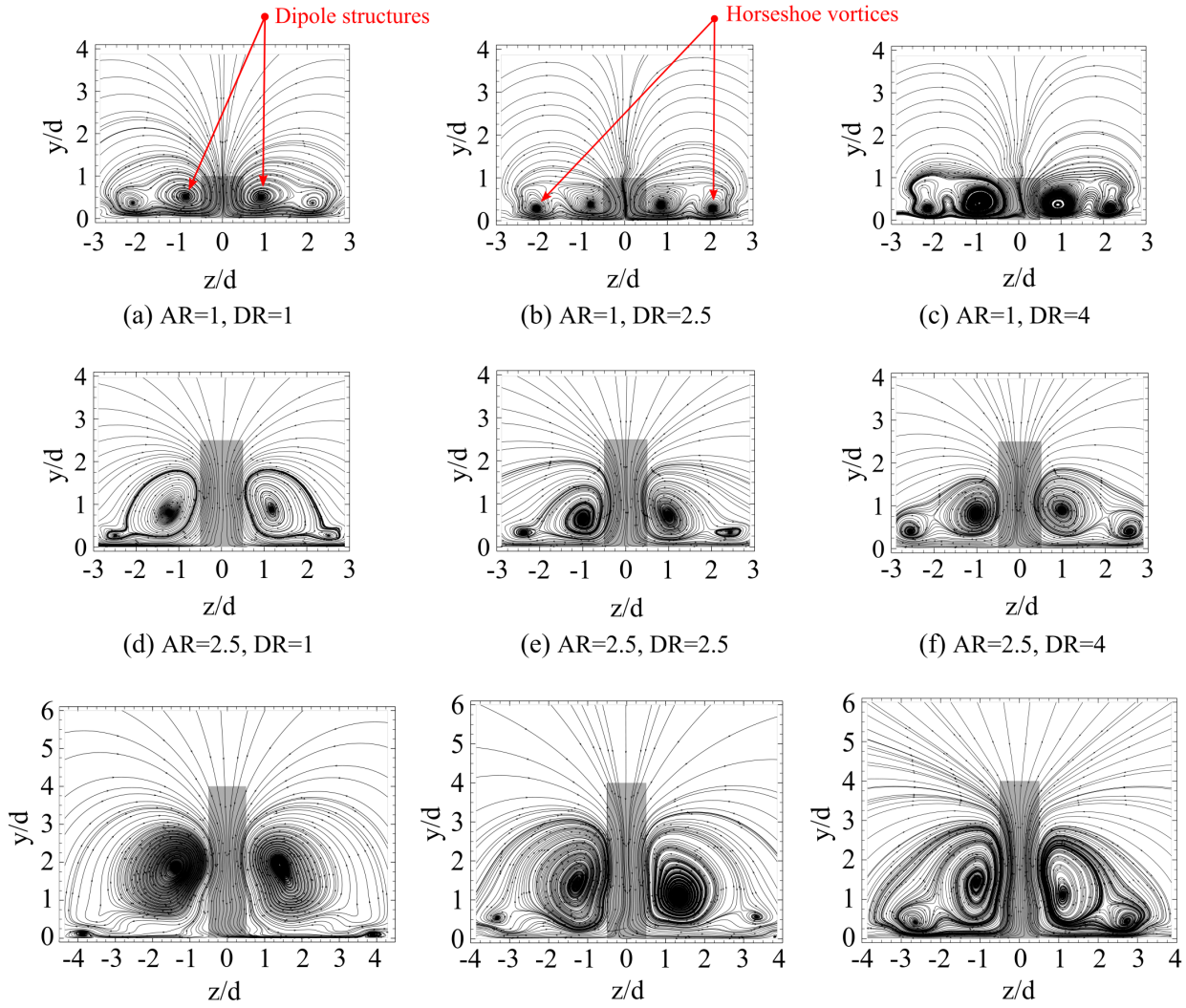

Figure 4.5: Mean streamlines at axial plane, $x/d = 7$, downstream of the cylinder from LES simulations.

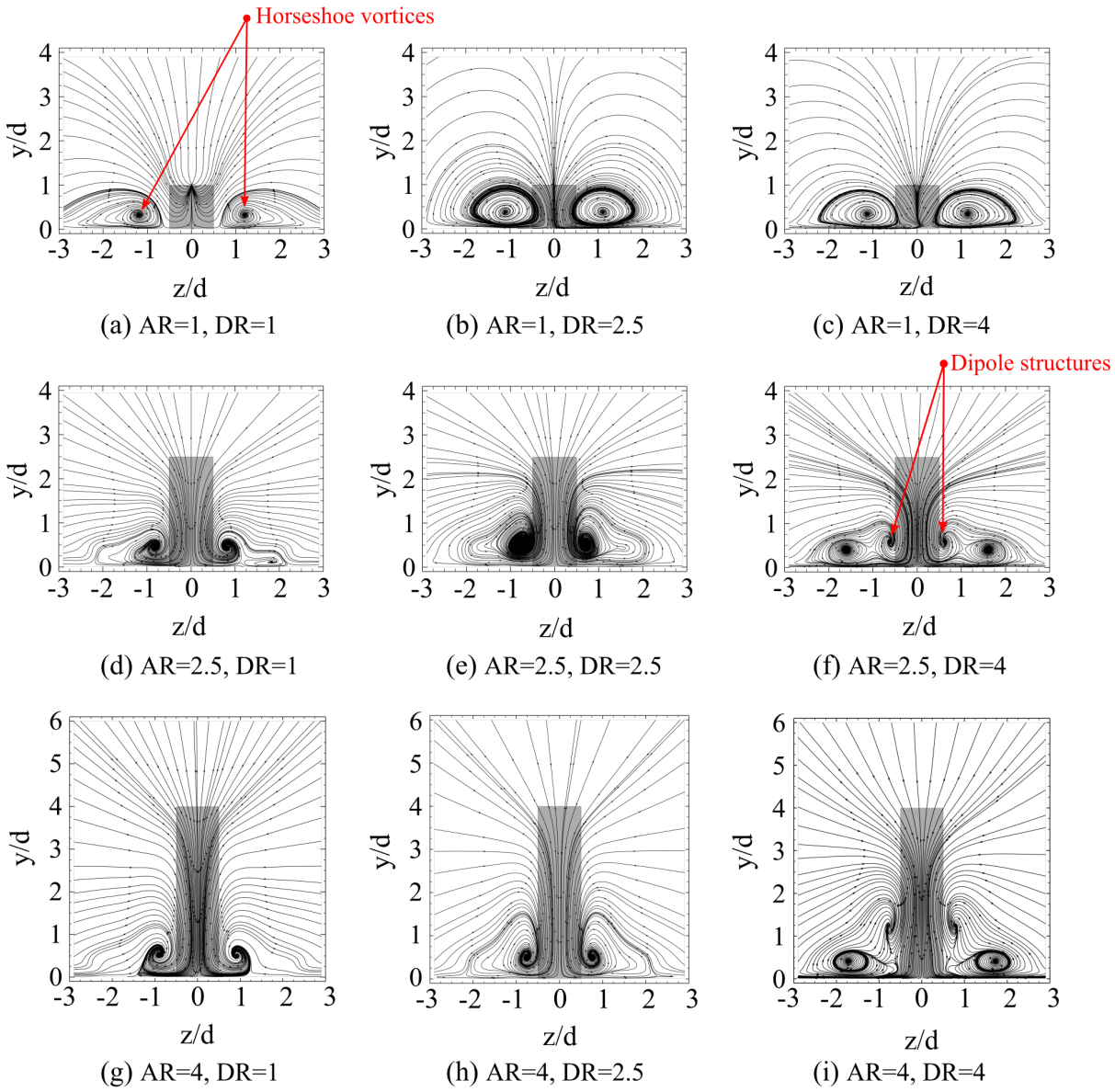

Figure 4.6: Mean streamlines at axial plane, $x/d = 7$, downstream of the cylinder from RANS simulations.

leads to flow reattachment on the cylinder top and side surfaces, which results in the suppression of tip vortex and reduction in strength of downwash flow (Goswami and Hemmati, 2022). The flow reattachment on the top surface of the cylinder initiated at $DR = 2$ for $AR \leq 1.5$, and $DR = 2.5$ for $AR \geq 2$, as noted in the presentation of LES results in Figure 4.7b. Consistent trends were observed in RANS results, while slight discrepancies were observed in cases of small aspect ratio and large depth-ratio cylinders. These discrepancies result from the inability of the RANS model to accurately predict the flow separation-reattachment on cylinder surfaces (Roy et al., 2003). In essence, RANS predictions followed similar trends to the LES results, with slight discrepancies. Further, the trends in X_R, X_T, and X_F satisfied the previous study on RANS performance on rectangular cylinders (Rodi, 1997; Roy et al., 2003; Tominaga, 2015).

Figure 4.8 shows the comparison of global (integral) flow variables, including mean drag force coefficient ($\overline{C}_d$), mean lift coefficient ($\overline{C}_l$), and mean base pressure coefficient ($\overline{C}_{bp}$). The results indicate a reduction in drag and lift coefficient with an increase in depth ratio at a particular aspect ratio. Further, increasing the aspect-ratio increases the drag on the cylinder, which remains consistent with Saha (2013). The $k - \omega$ SST model underpredicts both lift and drag coefficients. Further, the base pressure, i.e. the integral surface pressure on the leeward face of the cylinder, correlates with the estimation of drag (Hemmati et al., 2018). A plateau is observed in the base pressure coefficient with an increase in depth ratio, following which the base pressure increases. The plateau shifts to a larger depth ratio with an increase in aspect ratio, such that the plateau appears at $DR = 2$ for $AR = 1$, and at $DR = 3.5$ for $AR = 2.5$. While the $k - \omega$ SST model results follow the trends similar to LES, but it underpredicts the base pressure. The discrepancy in predicting the base pressure by the RANS model increases with increasing the aspect ratio. A similar trend is observed in the prediction of drag coefficient at larger aspect ratios. This hints at a correlation between base pressure and drag coefficient predictions. The major deviations in base pressure at large aspect ratios lead to underprediction of the mean drag coefficient. Past literature have indicated that the base pressure distributions are highly sensitive to complex and unsteady changes in the wake topology (Wang et al., 2006). An increase in the aspect ratio of the cylinder

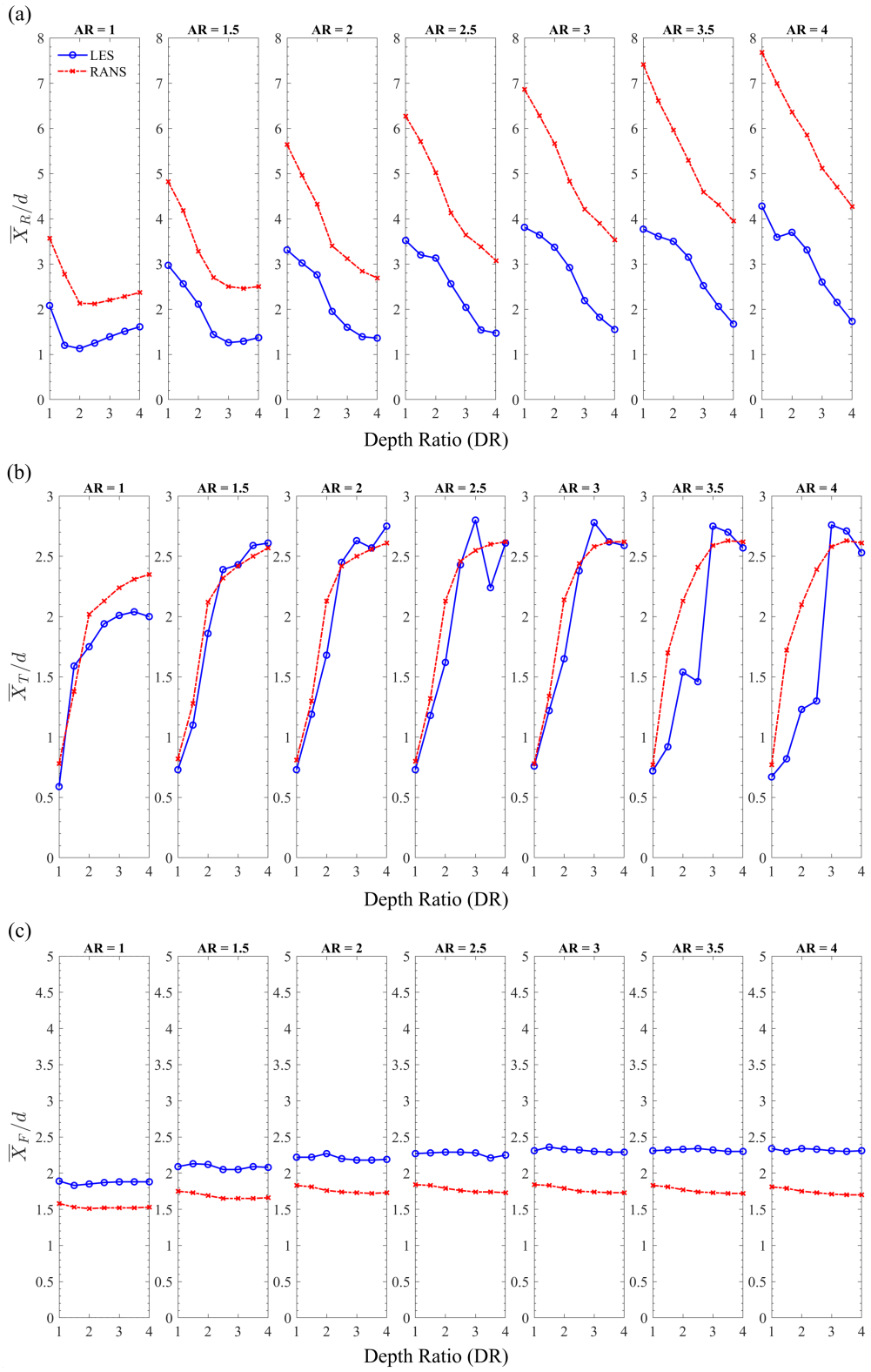

Figure 4.7: The variations of length of (a) reattachment region (X_R), (b) top recirculation (X_T), and (c) front separation region (X_F), with respect to AR and DR for all 49 cases in the time-averaged study.

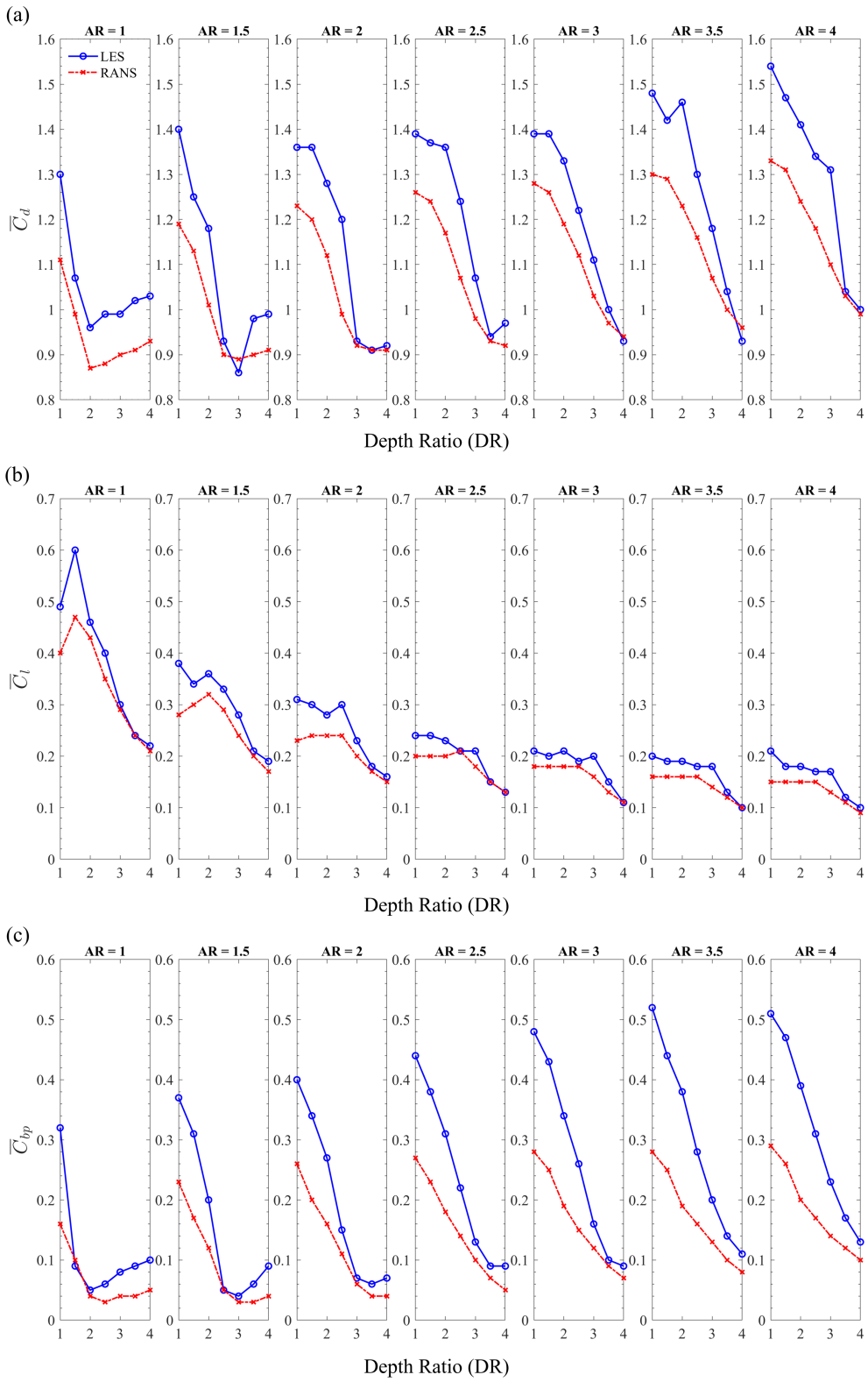

Figure 4.8: The variations of the mean (a) drag coefficient ($\overline{C}_d$), (b) lift coefficient ($\overline{C}_l$), and (c) base pressure coefficient ($\overline{C}_{bp}$), over the cylinders with respect to AR and DR for all 49 cases.

results in highly three-dimensional and complex wake structures behind the cylinder, which result in larger pressure and velocity gradients, especially in the vicinity of cylinder (Saha, 2013). The deviations in base pressure at higher aspect ratio cylinders, thus, indicate the limitations of this RANS model in predicting the flows under adverse pressure gradients.

Reynolds decomposition, which is utilized in RANS formulations, involves spliting the flow field into a mean and a fluctuating component. The turbulence kinetic energy (TKE) is defined as the mean of the square of the fluctuating velocity is often used as a measure of the intensity of turbulence. In order to predict TKE, RANS models make the following assumptions:

1. Reynolds decomposition: the velocity field is split into a mean and fluctuating component.

2. Local isotropy: turbulence is assumed to be isotropic (i.e., the same in all directions) and homogeneous (i.e., the same at all points) in the vicinity of the point where TKE is being predicted.

3. Local equilibrium: TKE is assumed to be in a state of balance between production and dissipation, and the production and dissipation are related through a closure model.

4. Reynolds Averaging: The equations are averaged over a time period that is long compared to the time scales of the turbulent fluctuations, but short compared to the time scales of the mean flow.

These assumptions allow RANS models to predict the TKE using relatively simple mathematical expressions, but they also introduce a degree of uncertainty into the predictions (Pope, 2000; Wilcox, 2006).

Figure 4.9 shows the terms of the TKE budget, including advection (A) by mean velocity, turbulence production (P) by shear, resolved dissipation (ϵ) , and viscous diffusion (D). These terms normalized by d and U_0. In $k-\omega$ SST (Menter, 1994) these terms become:

$$\underbrace{\frac{\partial(\rho u_j k)}{\partial x_j}}_{A} = \underbrace{\tau_{ij}\frac{\partial u_i}{\partial x_j}}_{P}\underbrace{-\beta^*\rho\omega k}_{\epsilon} + \underbrace{\frac{\partial}{\partial x_j}\left[(\mu+\sigma_k\mu_t)\frac{\partial k}{\partial x_j}\right]}_{D}, \tag{4.1}$$

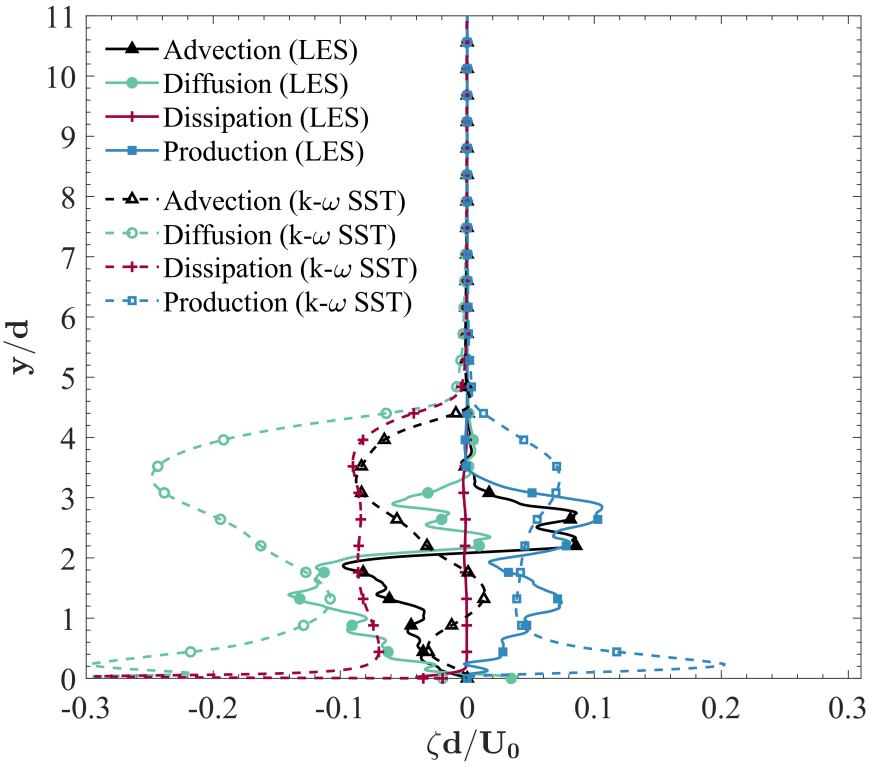

Figure 4.9: Comparison of the RANS model and LES turbulence kinetic energy terms for the cylinder with AR = 4, DR = 1 at $x/d = 5$ and $z/d = 0$ (ζ is a general variable).

In LES formulations (Pope, 2000), these terms become:

$$A = \overline{u_i}\frac{\partial k}{\partial x_i} = \frac{1}{2}\overline{u_i}\frac{\partial}{\partial x_i}(\overline{u_i' u_i'}), \tag{4.2}$$

$$P = -(\overline{u_i' u_j'} - 2\overline{\nu_\tau S_{ij}})\frac{\partial \overline{u_i}}{\partial x_j} = -\overline{u_i' u_j'}\frac{\partial \overline{u_i}}{\partial x_j} + 2\overline{\nu_\tau} S_{ij} S_{ij}, \tag{4.3}$$

$$\epsilon = 2\overline{\tau_{ij} S_{ij}} + 2\nu\overline{S_{ij} S_{ij}} \ . \tag{4.4}$$

For brevity, the results for only a representative cylinder with an aspect ratio of 4 and depth ratio of 1 is provided at $x/d = 5$ and $z/d = 0$. The results illustrate the difference between the two modeling approaches, which was consistently observed for all geometrical cases. Figure 4.9 shows the overestimation of dissipation rate and inaccurate prediction of the turbulence production by $k - \omega$ SST model compared to LES. These discrepancies come from the assumptions of the

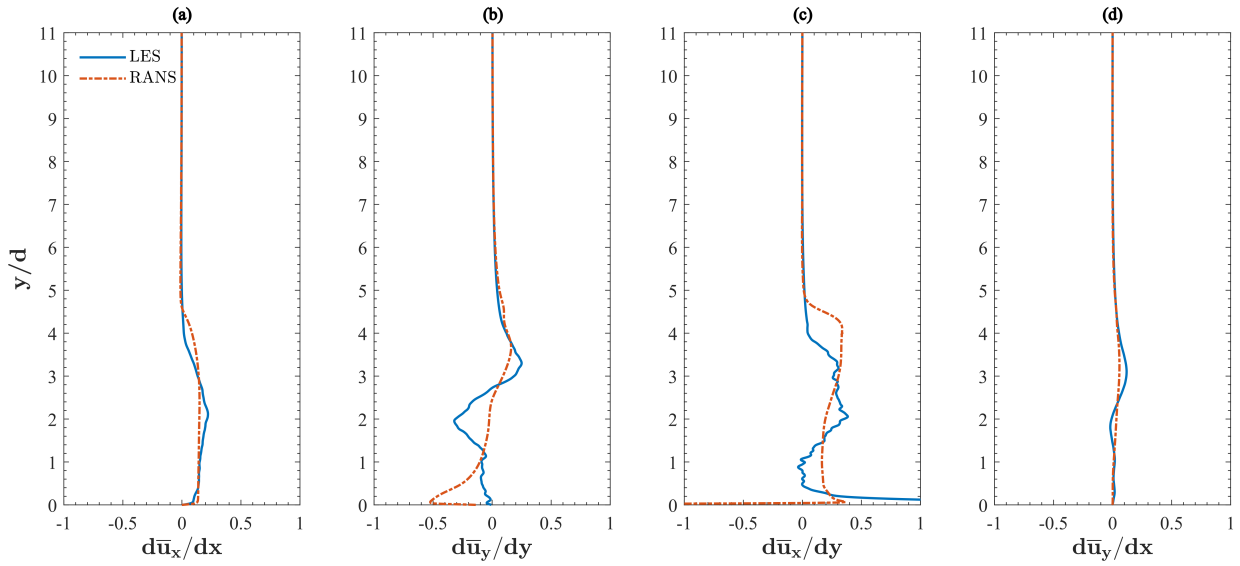

Figure 4.10: Comparison of the mean velocity gradient profile of (a) $d\overline{u}_x/dx$, (b) $d\overline{u}_y/dy$, (c) $d\overline{u}_x/dy$, and (d) $d\overline{u}_y/dx$ for the cylinder with AR = 4, DR = 1 at $x/d = 5$ and $z/d = 0$.

RANS equations. The overprediction of the diffusion term in this plot reveals that the artificial diffusion produced by the RANS model is used to stabilize the solution and prevent the formation of unphysical numerical oscillations. Moreover, the diffusive term added to the Reynolds stress tensor is often called the "viscous-like" or "diffusion-like" term and is intended to provide stability in regions of strong mean flow gradients, such as near walls and boundary layers (Wilcox, 2006). Furthermore, the advection term in the turbulence kinetic energy balance equation represents the transport of TKE by the mean flow. The advection term in LES and $k - \omega$ SST model is negative where the velocity is negative in the recirculation region and it becomes positive in the region with the positive velocity. The observation regarding the LES modeling of the TKE terms in figure 4.9 are consistent with the study of Ikhennicheu et al. (2020) using PIV measurements, and also the study of LES and DNS by Hemmati et al. (2018).

The velocity gradients, specifically the mean rate of strain and vorticity, are important for the prediction of turbulence kinetic energy. The mean rate of strain is defined as the rate of change of the velocity vector in a particular direction, and vorticity is defined as the curl of the velocity vector. In turbulent flows, the production of TKE is primarily due to the mean rate of velocity gradients and the Reynolds stresses are related to the fluctuations of momentum transport. This

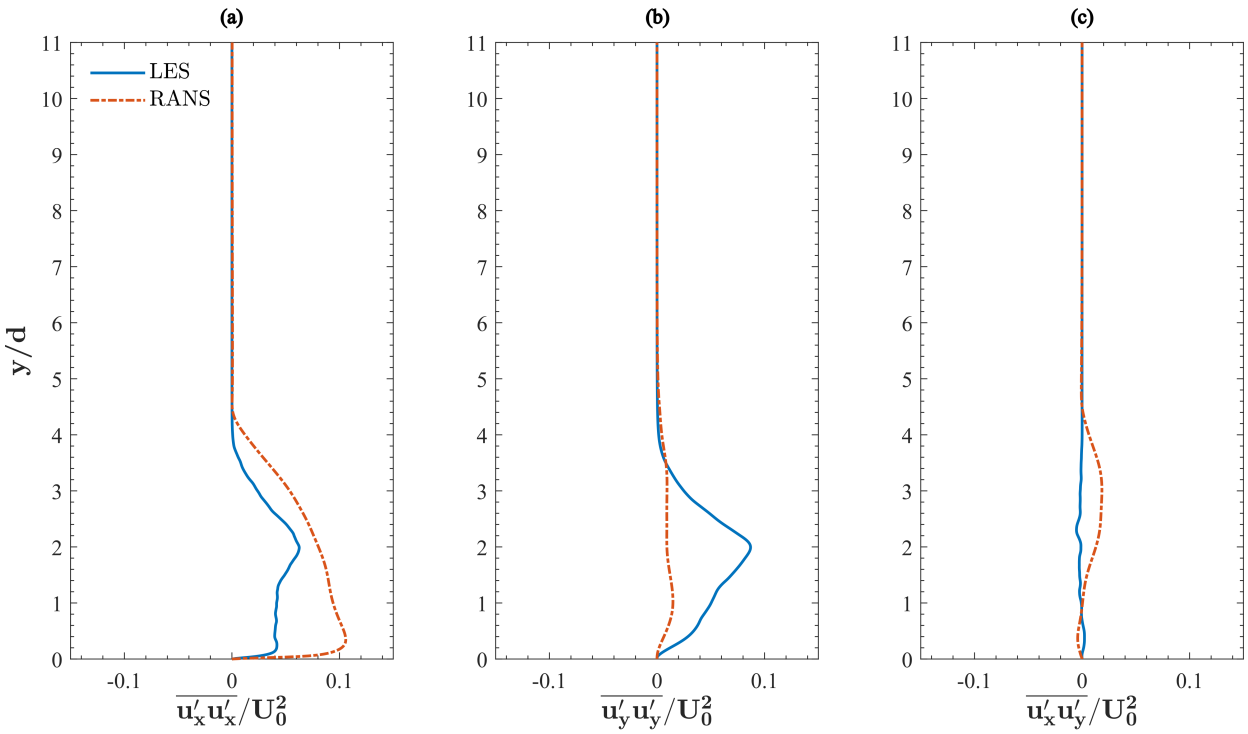

Figure 4.11: Comparison of the Reynolds stresses of (a) $\overline{u'_x u'_x}/U_0^2$, (b) $\overline{u'_y u'_y}/U_0^2$, and (c) $\overline{u'_x u'_y}/U_0^2$, for the cylinder with AR = 4, DR = 1 at $x/d = 5$ and $z/d = 0$.

interaction generates the turbulent velocity fluctuations that lead to the production of TKE (Pope, 2000). Figure 4.10 shows the inaccurate prediction of the gradient of velocity by $k-\omega$ SST model compared to LES for the representative cylinder. This is one reason for the inaccurate prediction of TKE production by the $k-\omega$ SST model.

Reynolds stresses shown in Figure 4.11, for the representative cylinder with an aspect ratio of 4 and depth ratio of 1 at $x/d = 5$ and $z/d = 0$, contain information about the turbulent fluctuations in the flow, including the turbulent kinetic energy, and the turbulent viscosity (Wilcox, 2006). Figure 4.11a presents the overestimation of normal Reynolds stress in the streamwise direction and Figure 4.11b shows the suppression of normal Reynolds stress in the vertical direction by $k-\omega$ SST model compared to LES. Furthermore, $k-\omega$ SST model underestimated the Reynolds shear stress ($\overline{u'_x u'_y}/U_0^2$) in Figure 4.11c near the lower wall at the bottom. It then overestimated this variable from near the middle height of the cylinder. The discrepancies between LES and $k-\omega$ SST model in the prediction of the Reynolds stresses, which play an important role in the

prediction of turbulence production term, coincide with the inaccurate prediction of TKE by this RANS model.

These serve as evidence of the $k-\omega$ SST model's limitation in effectively anticipating the wake properties, which have an impact on the mean flow field results. The overprediction of the velocity and underestimation of normal Reynold stress and poor prediction of turbulence kinetic energy terms by the RANS analysis lead to overprediction of the downwash flow and causes overprediction of reattachment length behind the cylinder known as wake region and other aforementioned discrepancies between RANS predictions and LES results.

The lack of accuracy in predicting flow features over rectangular cylinders by the $k-\omega$ SST model compared to LES mostly comes from the model of closure problem relates to the eddy viscosity hypothesis for modeling the Reynolds stresses in a linear correlation and the assumptions for the RANS decomposition. Furthermore, the lower accuracy is dependent on the relationships identified in the source terms of the Poisson equation, which will affect the correct prediction of the mean reattachment length, mean drag, and mean surface pressure (Fogaing et al., 2019; Hemmati et al., 2019). Finally, these inaccuracies are linked to discrepancies in predicting the velocity and pressure gradients in the wake, especially with increasing aspect ratio. For an illustration of the RANS limitations, the Reynold stresses, and mean velocity of a representative case are compared.

Since the estimation of upwash and downwash flow determines the wake dynamics for finite, wall-mounted cylinders, we look at the trends of mean normal Reynolds stress ($\overline{u'_y u'_y}/U_0^2$) for the case of the cylinder with an aspect ratio of 4 and depth-ratio of 1 in Figures 4.12a, and 4.12b. Since the trends in all cases are similar, the results for other cases are omitted for brevity. The results indicate a significant suppression of $\overline{u'_y u'_y}/U_0^2$ by the RANS model, while a prolonged momentum transfer by $\overline{u'_y u'_y}/U_0^2$ is observed for LES. In the case of LES, the concentration of $\overline{u'_y u'_y}/U_0^2$ (red-coloured region) corresponds to the downwash flow induced by the tip-vortex. In addition, $\overline{u'_y u'_y}/U_0^2$ transports downstream till $x/d \approx 10$, and corresponds to the tip vortex in the downstream wake, as shown in Figure 4.3g. The transport of Reynolds stresses is associated with the formation of spanwise vortices, $i.e.$ the tip and base vortices, and their convection downstream in the

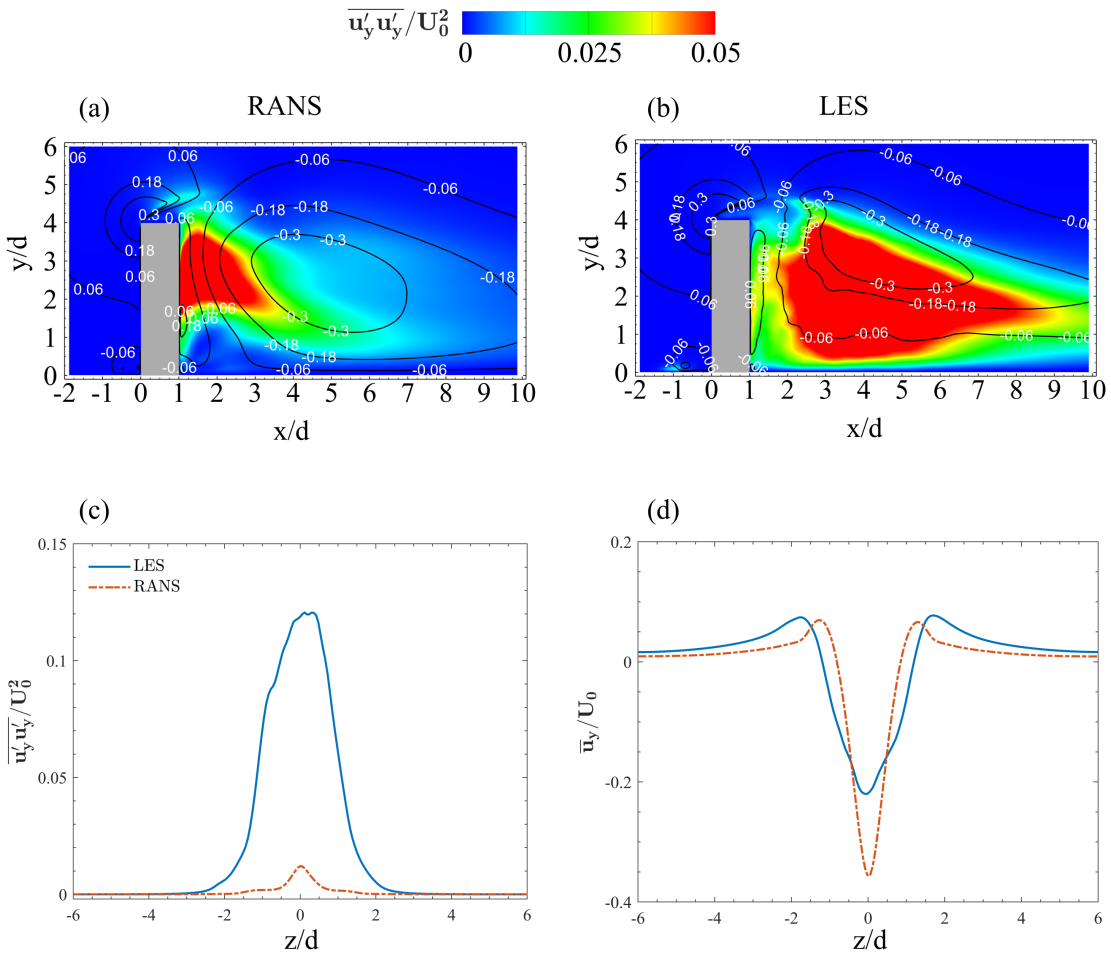

Figure 4.12: Comparison of normal Reynolds stress $\overline{u_y' u_y'}/U_0^2$ in coloured contours and $\overline{u}_y/U_0$ in the line contours at xy-plane and $z/d = 0$ for (a) RANS and (b) LES. The profile for RANS and LES of (c) normal Reynolds stress and (d) y-velocity at $x/d = 5$ and at the middle height of the cylinder AR = 4 and DR = 1.

wake (More et al., 2015). The $k-\omega$ SST model, instead, predicts a suppression of $\overline{u'_y u'_y}/U_0^2$ in the downstream vicinity of the cylinder with a transport closer to the ground at $x/d = 5$. Further, the suppression of stresses in the RANS model is observed in the spanwise plane, shown in Figure 4.12c, which results in a narrower wake compared to that obtained by LES and shown in Figure 4.12d. In the case of LES, the transport towards the ground is prolonged till $x/d > 10$. The transport of stresses towards the ground correlates with the location of tip-vortices (see Figure 4.6g) closer to the ground in the case of the RANS model. Thus, the discrepancy noted in the wake topology by the RANS model results from its inability to correctly predict the momentum transport due to stresses. These observations are consistent with the findings of Fogaing et al. (2019).

Chapter 5

CORRECTION OF SIMULATION RESULTS

In this chapter, a machine learning algorithm is developed to correct the mean wake characteristics and the global features simulated by RANS $k-\omega$ SST model over the wall-mounted rectangular cylinders. Quantitative parameters are employed for training the neural network algorithm described in Chapter 3. The parameters of the main flow features and global quantities are compared to indicate the discrepancies in the prediction of these parameters by the $k-\omega$ SST model compared to LES. Finally, performance of the trained neural network associated with predictions for the current data and unseen data is presented.

5.1 Numerical simulations data

The performance of $k-\omega$ SST model in simulating the flow around wall-mounted cylinders at $\mathrm{R}e_d = 2.5 \times 10^3$ was evaluated in Chapter 4. While comparing different flow and wake parameters obtained by the RANS model and LES, it was revealed that there are systematic trends in over- and under-predictions of these parameters in modeling with $k-\omega$ SST. This hinted at a similar approach in correcting these results, based on more accurate reference data, i.e. LES results. Thus,

a neural network algorithm is introduced here that corrects $k-\omega$ SST model results of the flow around wall-mounted cylinders using LES results.

Figures 5.1 shows the discrepancies between the $k-\omega$ SST results in the estimation of the mean wake parameters compared with LES results with respect to the changing aspect ratio and depth ratio of the cylinders. At the right-hand side of Figure 5.1, an example is provided of each plot, which shows the mean velocity streamlines at the cylinder spanwise middle plane, $z/d = 0$. The reattachment length behind the cylinder (X_R), located downstream of the domain (the near-wake region), is represented in Figure 5.1a. The reattachment length is created by the separated flow at the leading edges of the cylinder, which reattaches to the cylinder downstream (Sarpkaya and Issa, 1981). X_R is an important parameter in fluid dynamics, as it can affect the drag and lift forces acting on the body, as well as the overall flow field (Savory and Driver, 1994; Gao and Rodi, 1998). Figure 5.1a indicates that the $k-\omega$ SST model significantly overpredicted the reattachment length (X_R). Despite this overprediction, it follows the same pattern as the LES results. Increasing the aspect ratio leads to increasing X_R because the flow stream behind the cylinder from the bottom to the top (upwash flow) dominates the flow coming from the free end downward (downwash flow) (Wang and Zhou, 2009). As the depth ratio increases, the downwash flow weakens and causes X_R to increase (Goswami and Hemmati, 2022). Figure 5.1b presents the front recirculation length (X_F) associated with the formation of the horseshoe vortex and how it embraces the cylinder. Since the size of the horseshoe vortex greatly depends on the thickness of the boundary layer upstream of the cylinder, no substantial variation in X_F is noticed with changing aspect ratio and depth ratio (Hwang and Yang, 2004). Further, the top recirculation length (X_T) is shown in Figure 5.1c. The leading edge flow separation is responsible for the formation of the top recirculation zone. As the depth ratio goes up, an adverse-pressure gradient occurs on the top surface of the cylinders, causing the flow to rejoin the surface (Zargar et al., 2021). Finally, the observed trends in X_R, X_T, and X_F are in good agreement with the results of earlier studies of RANS performance on the flow around wall-mounted rectangular cylinders (Rodi, 1997; Roy et al., 2003; Tominaga, 2015).

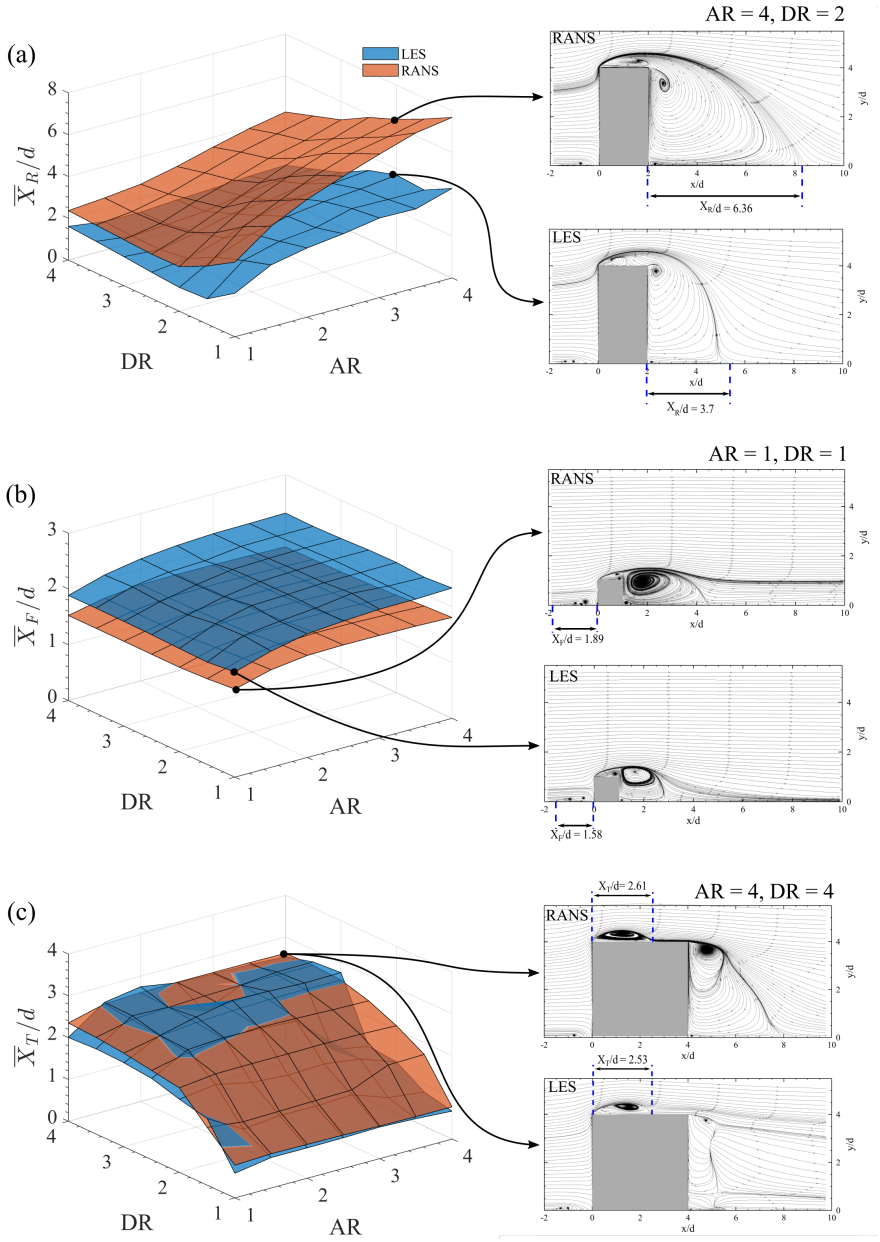

Figure 5.1: Comparison of RANS and LES data: (a) reatachment lenght, (b) front separation length, and (c) top recirculation length.

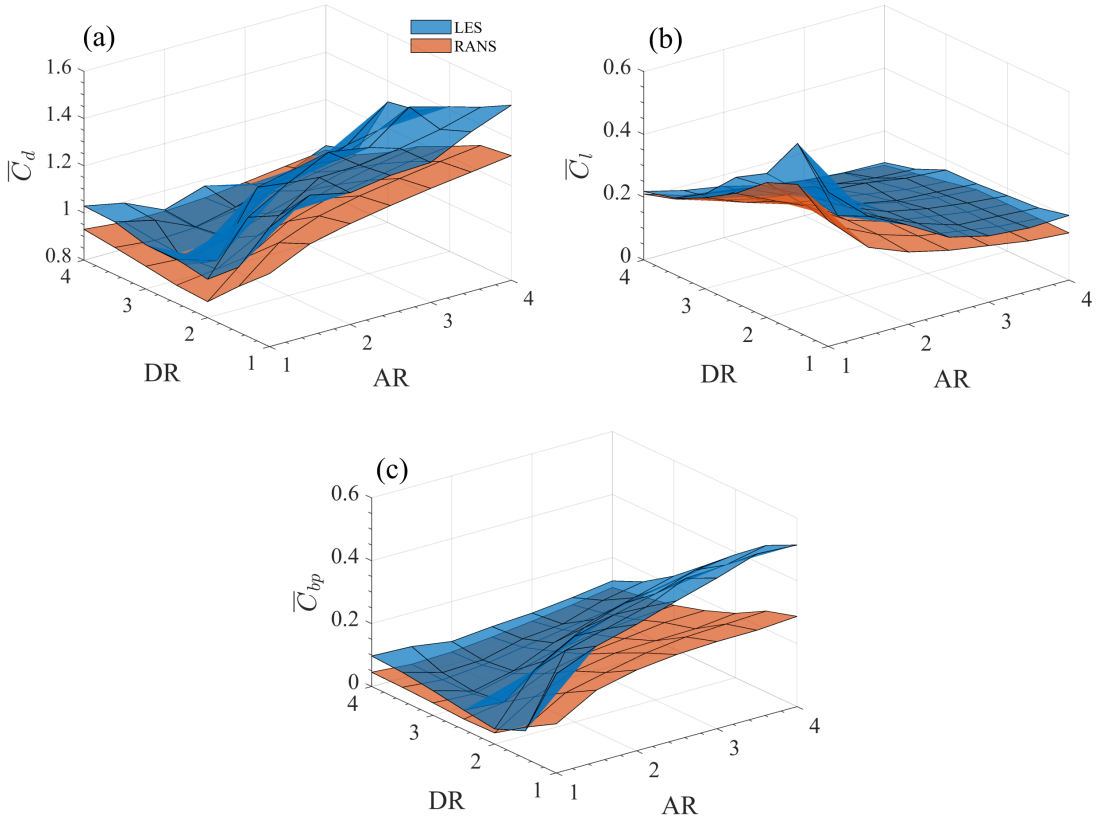

Figure 5.2: Comparison of RANS and LES data (a) mean drag force coefficient, (b) mean lift force coefficient, and (c) mean base pressure coefficient.

Figure 5.2 presents the comparison of the global parameters of the mean flow of the wall-mounted cylinders obtained from the $k-\omega$ SST model and LES results. Figure 5.2a demonstrates the mean drag force coefficient ($\overline{C}_d$), defined as a dimensionless parameter to evaluate the mean force on the cylinder in the streamwise direction. The mean lift force coefficient ($\overline{C}_l$) is shown in Figure 5.2b, representing the forces in the normal (vertical) direction. The results show that while the depth ratio increases at a particular aspect ratio, the drag and lift coefficients decrease. Additionally, raising the aspect ratio enhances the drag force on the cylinder, which is consistent with earlier work of Saha (2013).

The mean base pressure coefficient ($\overline{C}_{bp}$) in Figure 5.2c indicates the integral surface pressure on the leeward face of the cylinder. Moreover, at the results in Figures 5.2a and 5.2c, it revealed that the base pressure and drag coefficient are related to each other (Hemmati et al., 2018). Ac-

cordingly, a larger cylinder aspect ratio produces highly complex, three-dimensional wake patterns behind the cylinder, which increases pressure and velocity gradients, thereby increasing the base pressure (Saha, 2013). Comparison of the global parameters results from the $k-\omega$ SST model and LES in Figure 5.2 indicates that the former underpredicted all three parameters ($\overline{C}_d$, $\overline{C}_l$, and $\overline{C}_{bp}$). However, the employed RANS model has the same trend as LES in predicting the global parameters of the mean flow around the wall-mounted cylinders. This implies that the RANS model succeeds in capturing the wake topology correctly.

5.2 Artificial neural network algorithm

A neural network algorithm was employed to improve the accuracy of key parameters from the RANS model. Collecting and preparing a dataset for the neural network in training constitutes the first step in this process. The dataset should include input data as well as the appropriate outputs for the task that the network is being trained to complete. Here, the objective for the correction of data from the $k-\omega$ SST model is to enhance the accuracy of the post-processed results, specifically regarding the prediction of the quantitative mean wake characteristics and global mean flow parameters using LES results. The backpropagation multi-layer perceptron neural network was trained by 49 data sets from numerical simulations on key parameters: X_R, X_T, X_F, $\overline{C}_d$, $\overline{C}_l$, and $\overline{C}_{bp}$. Figures 5.1 and 5.2 show that except, for front recirculation and reattachment length parameters, there is a nonlinear relationship between parameters predicted by $k-\omega$ SST model and by LES. To this end, the artificial neural network was utilized because of the existence of nonlinear activation functions in the neurons, which allows the model to learn and represent more complex and nuanced relationships in the data. The implemented neural network consists of 5 layers, including 3 hidden layers and 2 input and output layers. The input units are the RANS data, aspect ratio, and depth ratio, along with LES results as the target and high-quality data. Next, the algorithm (hypothesis function), including weights in the output layer generates the predicted data. Meanwhile, it is crucial to assess performance of the neural network model on two separate datasets (validation

set and test set) after training to make sure the model is generalizing successfully to new data. This is accomplished by evaluating the predicted outputs for the datasets with the actual results, as described in Chapter 3. In this chapter, performance of the trained neural network algorithm is evaluated for the current data and some unobserved data to make sure the algorithm performs well in correcting these wake parameters predicted by the $k-\omega$ SST model.

Figure 5.3 shows the performance of the algorithm to approximate all the data compared to the target in the regression plot. Regression plots are a frequent way to show the effectiveness of a trained machine-learning algorithm in earlier research (Hanna et al., 2020; Lin et al., 2021). A regression plot is a graphical representation of the relationship between two variables. It is used to visualize the strength and direction of the relationship between the variables, as well as to identify any potential outliers or unusual observations. In addition, the correlation coefficient (R) determines the degree and direction of the relationship between the two variables being plotted. Moreover, the correlation coefficient (R) is a statistical measure with a range of -1 to 1, with values closer to 1 implying a significant positive relationship, values closer to -1 representing a strong negative relationship, and values closer to 0 indicating a weak or no correlation. The data must fall on a 45-degree line, where the network outputs and responses are equal, for a perfect match. For this study, Figure 5.3, the red dashed line is the independent actual data and the blue circles are scattered related to the predicted data by the trained neural network including the data sets, such as test data, validation data, and training data. While the validation data is used to assess the degree of the polynomial, the test data is utilized for unseen data to evaluate the generalization performance of the algorithm, and the training data trains the algorithm and optimize the weights (a detailed explanation is given in Chapter 3). Figure 5.3 shows that there is no remarkable outlier, and the entire data sets with correlation coefficient R ≈ 1 in matching well.

Figure 5.4 indicates the proficiency of the trained neural network to predict each parameter. Individual regression plots assist in evaluating each parameter separately and in tuning the algorithm either by modifying the optimization method or its hyperparameters, modifying the design of the model or collecting and utilizing more training data. As it is shown, the plots contain the RANS

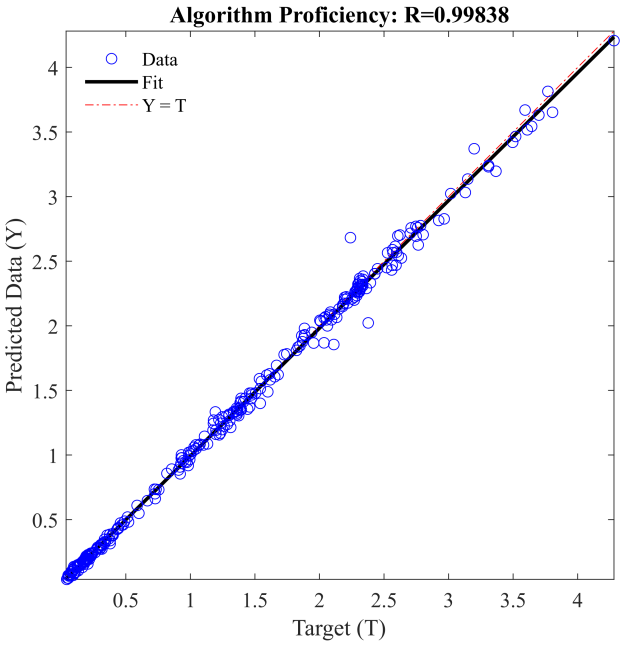

Figure 5.3: Algorithm performance regression plot for validation, test, and training data.

data as the low accuracy simulation, the LES data as the high accuracy and reliable data, and the predicted data that shows the estimation of the neural network algorithm. The correlation coefficients in Figures 5.4a, 5.4c, and 5.4f, show that the $k-\omega$ SST model results are properly corrected in terms of reattachment length (X_R) behind the cylinder, recirculation length (X_T) on top of the surface of the cylinder, and pressure coefficient ($\overline{C}_{bp}$) corresponding to the maximum pressure on the leeward surface of the cylinder. Furthermore, the mean drag coefficient and the mean lift coefficient in Figures 5.4d and 5.4e, respectively, have $R \approx 0.98$ that is still a high-quality performance for the trained neural network. Figure 5.4b demonstrates the lowest relation between predicted data and the actual data ($R \approx 0.97$) for the front recirculation length (X_F) parameter. To address the deficit for the correlation coefficient, it is observed in Figure 5.1b that there is no remarkable variation. In contrast, the multi-layer neural network performs better for nonlinear and complex problems, thus the weights are modified for X_F in the optimal method. Additionally, Figure 5.4 shows that there are no significant outliers in regression plots. Consequently, Figures 5.3 and 5.4 indicate that the neural network approach was successfully trained for enhancing the accuracy of

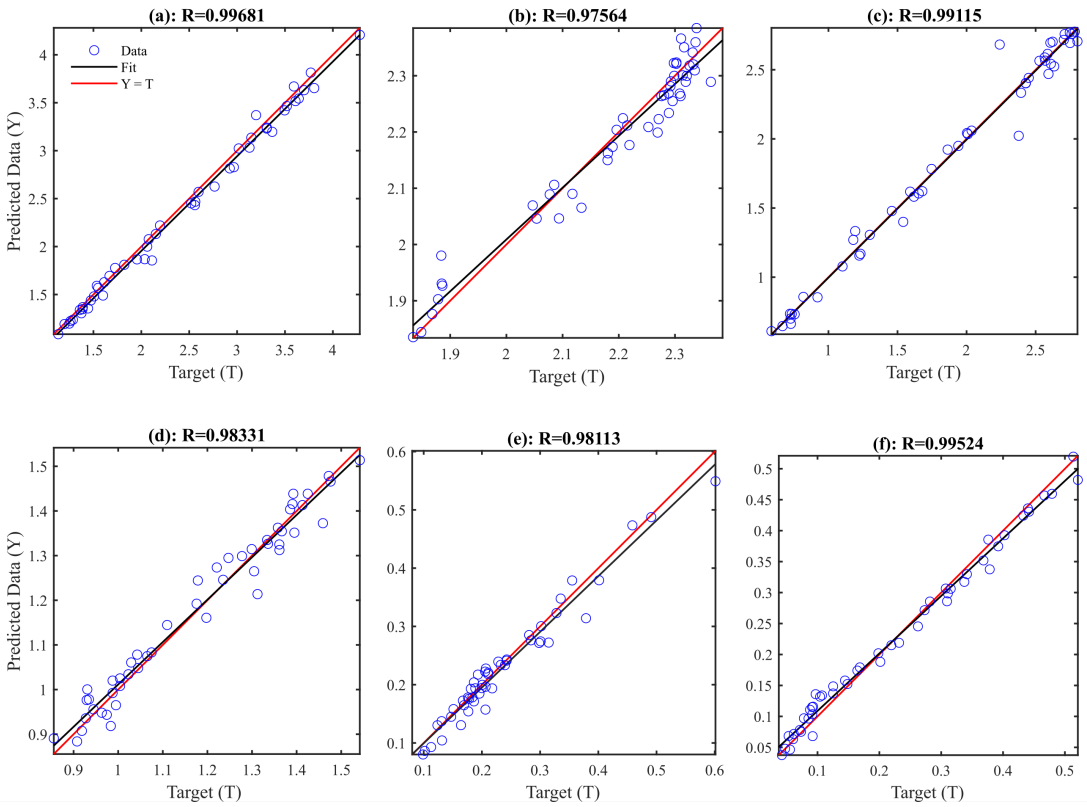

Figure 5.4: Regression plot of parameters (a) reattachment length (X_R), (b) front separation length (X_F), (c) top recirculation length (X_T), (d) mean drag coefficient ($\overline{C}_d$), (e) mean lift coefficient ($\overline{C}_l$), and (f) mean base pressure coefficient ($\overline{C}_{bp}$).

the approximations in the RANS $k-\omega$ SST model for the specified parameters within the current and unseen data ranges.

5.3 Independent verification and validation study

Independent verification and validation studies are used to evaluate the efficiency of a machine learning model when applied to new data that was not used throughout the training. An independent study aims to guarantee that the model generalizes appropriately to new data and it is not overfitting to the training data. Thus far, the neural network effectively enhances the accuracy of the predicted wake characteristics by the $k-\omega$ SST model using LES data for the flow over wall-mounted rectangular cylinders with aspect ratio and depth ratio from 1 to 4 at $\mathrm{Re}_d = 2.5 \times 10^3$.

X_R/d	**Actual**	**RANS**	**ANN**	$\|\Delta RANS\|\,\%$	$\|\Delta ANN\|\,\%$	**Improvement%**
Case 1	2.82	3.96	2.77	40.42	1.77	95.62
Case 2	1.63	3.56	2.07	118.4	12.69	89.28
Case 3	4.29	6.10	4.10	42.19	4.42	89.52

Table 5.1: Comparison of the reattachment length for cases 1, 2, and 3 in actual, RANS, and output data of the neural network algorithm.

Even though the algorithm already had test data to assess generalization error, an independent test was conducted for three more cases where actual results (experimental or DNS) exist for comparison. Case 1 is a DNS study of a cube at $\mathrm{Re}_d = 3 \times 10^3$ (Diaz-Daniel et al., 2017), case 2 is a new cylinder size with AR =1 and DR = 0.5 at $\mathrm{Re}_d = 2.5 \times 10^3$, and case 3 is the same validation case for this study with AR =4 and DR = 1 at $\mathrm{Re}_d = 1.2 \times 10^4$ (Saeedi et al., 2014). The RANS analysis of the three cases has been done and was imported to the algorithm for transformation. Only the recirculation length parameter behind the cylinder is compared, since that was the only parameter reported in three independent studies. Table 5.1 shows the value of the reattachment length for these cases, including actual data collected from the independent studies, RANS data, and predicted data exported from the trained artificial neural network. In addition, the percentage difference between the actual data and predicted data of RANS model ($|\Delta RANS|\,\%$), as well as the percentage difference between the actual data and the predicted data of the algorithm ($|\Delta ANN|\,\%$) are given in Table 5.1. The extracted reattachment length from DSN study in Case 2 led to a large discrepancy between actual data and predicted data since the reattachment length is overpredicted by LES compared to DNS (Hemmati et al., 2018). Finally, the last column in Table 5.1 presents improvements of the trained algorithm in predicting the results compared to the original low-accuracy $k-\omega$ SST model. The neural network prediction error compared to the error of the RANS model is significantly lower and the level of accuracy improvement is also satisfactory. This implies that the trained neural network algorithm successfully improved the $k-\omega$ SST model in terms of the unobserved data parameters over wall-mounted rectangular cylinders.

Chapter 6

CONCLUSIONS

The performance of the RANS ($k-\omega$ SST) model in simulating the flow features around wall-mounted finite rectangular cylinders was evaluated by comparing the results with those of the corresponding LES simulations. This revealed similarities in the prediction of mean flow global features and wake characteristics and their trends over wall-mounted rectangular cylinders. In particular, the main characteristic flow features, such as shear-layer separation, recirculation, and reattachment over cylinders were successfully captured by the RANS model. Moreover, the RANS model successfully predicted the main components of the wake topology, such as the tip, base, and horseshoe vortices. Nonetheless, there were significant discrepancies in the mean flow features, mean wake structures, and global features of mean flow compared to LES:

- The reattachment length behind the cylinder (X_R) decreased with increasing aspect ratio and increased with decreasing depth ratio. A larger depth ratio led to a stronger downwash flow, which results in shrinking of the recirculation zone behind the cylinder. Further, an increase in aspect ratio caused the upwash flow to dominate at a certain depth ratio, which expanded the recirculation zone. However, the RANS model significantly overestimated the value of X_R, despite succeeding in capturing the correct flow topology.

- The recirculation length (X_T) on the top surface of the cylinder grew with increasing depth ratio. And an adverse-pressure gradient formed on the top surface of the cylinder, causing the

flow to reattach to the surface. Further, LES simulations revealed that the flow reattachment on the top surface of the cylinder started at $DR = 2$ for $AR \leq 1.5$ and $DR = 2.5$ for $AR \geq 2$. In this case (with a few minor exceptions) the $k-\omega$ SST model essentially follow the same trends as LES in terms of estimating X_T over wall-mounted rectangular cylinders.

- The horse-shoe vortex in front of the cylinder strongly depends on the thickness of the upstream boundary layer. Therefore, no significant variation in the recirculation length is seen in front of the cylinder (X_F) with changing aspect ratio and depth ratio. Although, the $k-\omega$ SST model followed the same trend as LES in predicting X_F with respect to changing aspect ratio and depth ratio, it underpredicted the value of X_F compared to LES.

- The comparison of global (integral) flow variables between LES and $k-\omega$ SST model, including mean drag force coefficient ($\overline{C}_d$), mean lift coefficient ($\overline{C}_l$), and mean base pressure coefficient ($\overline{C}_{bp}$), showed that the $k-\omega$ SST model underpredicted these coefficients. However, the RANS model predicted the global flow variables with a similar pattern as LES.

- LES simulation results showed the formation of the tip and base vortices as well as the horseshoe vortex for all cases. The horseshoe and tip vortices extended in the downstream wake and then formed the dipole-type structure. RANS models, however, did not capture these vortices behind the cylinder. Correspondingly, the tip vortex becomes more intense with increasing aspect ratio. Increasing the depth ratio led to the shear layer reattachment to the top surface of the cylinder, which then forces the trailing edge to separate. Furthermore, increasing the depth ratio suppressed the downwash flow, which distorted the tip vortex. Therefore, it was essential to predict the tip vortex accurately in the downstream wake region to capture the wake features correctly.

- The formulation of the RANS $k-\omega$ SST model, which is based on the eddy viscosity hypothesis in modeling the Reynolds stresses in a linear correlation, is the primary reason for the RANS model's error in predicting flow features over rectangular cylinders. Comparison

of the mean normal Reynolds stresses indicated that the $k-\omega$ SST model significantly underestimated the Reynolds stresses and considerably suppressed it in the near wake region.

A backpropagation multi-layer perceptron artificial neural network algorithm was developed and introduced to correct key wake parameters modeled by the RANS $k-\omega$ SST model. The trained neural network algorithm specifically enhanced the accuracy of these mean wake quantitative parameters, including the reattachment length behind the cylinder, the recirculation length in front of the cylinder, the top recirculation length, the mean drag coefficient, the mean lift coefficient, and the mean base pressure coefficient. The algorithm was trained using LES data for 49 wall-mounted rectangular cylinders with different aspect ratios and depth ratios ranging from 1 to 4, at $\mathrm{Re}_d = 2.5 \times 10^3$. results from the performance of the neural network algorithm showed that the algorithm effectively corrects these parameters simulated by the $k-\omega$ SST model compared to the actual values. Furthermore, in both the current and unseen data ranges, the neural network technique was successfully trained to improve the RANS $k-\omega$ SST model results for the given parameters in the study of flow around wall-mounted rectangular cylinders.

RANS-based turbulence modeling is a widely used approach in the industry for analyzing and designing different engineering systems. The trained machine-learning algorithm in this study effectively improved the flow parameters predicted by the $k-\omega$ SST model towards the same accuracy of computationally expensive techniques. The results indicate that a RANS numerical model can estimate the fundamental flow characteristics over wall-mounted rectangular cylinders with relatively low computation cost. Although many studies have tried to resolve the limitations of the RANS simulation by enhancing their formulations, the present study was one of the first to employ machine learning for improvement of post-processed results. The considerable advantage of the trained algorithm is its ability to include more data in the future based on changes in Reynolds numbers, boundary layer thickness, and shapes of bluff bodies at a relatively low computational cost.

Bibliography

Anderson, J. D. (1990). *Modern compressible flow: with historical perspective*, volume 12. McGraw-Hill New York.

Batchelor, C. K. and Batchelor, G. (2000). *An introduction to fluid dynamics*. Cambridge university press.

Blocken, B. (2018). LES over RANS in building simulation for outdoor and indoor applications: A foregone conclusion? *Building Simulation*, 11:821–870.

Bonaccorso, G. (2018). *Machine learning algorithms : popular algorithms for data science and machine learning*. Packt Publishing.

Bonaccorso, G. (2020). *Mastering machine learning algorithms : expert techniques for implementing popular machine learning algorithms, fine-tuning your models, and understanding how they work*. Packt Publishing.

Bourgeois, J. A., Sattari, P., and Martinuzzi, R. J. (2011). Alternating half-loop shedding in the turbulent wake of a finite surface-mounted square cylinder with a thin boundary layer. *Physics of Fluids*, 23:095101.

Brunton, S. L., Noack, B. R., and Koumoutsakos, P. (2020). Machine learning for fluid mechanics. *Annual Review of Fluid Mechanics*, 52(1):477–508.

Calzolari, G. and Liu, W. (2021). Deep learning to replace, improve, or aid CFD analysis in built environment applications: A review. *Building and Environment*, 206:108315.

Cappelli, D. and Mansour, N. N. (2013). Performance of reynolds averaged navier-stokes models in predicting separated flows: study of the hump flow model problem. In *31st AIAA Applied Aerodynamics Conference*, page 3154.

Castro, I. P. and Robins, A. G. (1977). The flow around a surface-mounted cube in uniform and turbulent streams. *Journal of Fluid Mechanics*, 79:307–335.

Celik, I., Klein, M., and Janicka, J. (2009). Assessment measures for engineering LES applications. *Journal of Fluids Engineering*, 131.

Cheng, Y., Lien, F., Yee, E., and Sinclair, R. (2003). A comparison of large eddy simulations with a standard $k-\epsilon$ reynolds-averaged navier–stokes model for the prediction of a fully developed turbulent flow over a matrix of cubes. *Journal of Wind Engineering and Industrial Aerodynamics*, 91:1301–1328.

da Silva, B. L., Chakravarty, R., Sumner, D., and Bergstrom, D. J. (2020). Aerodynamic forces and three-dimensional flow structures in the mean wake of a surface-mounted finite-height square prism. *International Journal of Heat and Fluid Flow*, 83:108569.

Davidson, L. (2020). Fluid mechanics, turbulent flow and turbulence modeling. *Chalmers University of Technology, Goteborg, Sweden*.

Diaz-Daniel, C., Laizet, S., and Vassilicos, J. (2017). Direct numerical simulations of a wall-attached cube immersed in laminar and turbulent boundary layers. *International Journal of Heat and Fluid Flow*, 68:269–280.

Dimaczek, G., Tropea, C., and Wang, A.-B. (1989). Turbulent flow over two-dimensional, surface-mounted obstacles: plane and axisymmetric geometries. In *Advances in Turbulence 2*, pages 114–121. Springer.

Durbin, K. and Baeder, J. (2013). A review of hybrid RANS/LES approaches for aerodynamic simulations. *Progress in Aerospace Sciences*, 64:1–38.

Durbin, P. A. and Reif, B. P. (2011). *Statistical theory and modeling for turbulent flows. John Wiley and Sons.*

Fogaing, M. B. T., Hemmati, A., Lange, C. F., and Fleck, B. A. (2019). Performance of turbulence models in simulating wind loads on photovoltaics modules. *Energies*, 12:3290.

Gao, J. and Rodi, W. (1998). Reattachment length for flow past a circular cylinder at high angles of attack. *Journal of Fluids and Structures*, 12(5):643–659.

Geneva, N. and Zabaras, N. (2019). Quantifying model form uncertainty in reynolds-averaged turbulence models with bayesian deep neural networks. *Journal of Computational Physics*, 383:125–147.

Goodfellow, I., Bengio, Y., and Courville, A. (2016). *Deep Learning*. MIT Press.

Goswami, S. and Hemmati, A. (2020). Response of turbulent pipeflow to multiple square bar roughness elements at high reynolds number. *Physics of Fluids*, 32(7):075110.

Goswami, S. and Hemmati, A. (2022). Mechanisms of wake asymmetry and secondary structures behind low aspect-ratio wall-mounted prisms. *Journal of Fluid Mechanics*, 950:A31.

Hanna, B. N., Dinh, N. T., Youngblood, R. W., and Bolotnov, I. A. (2020). Machine-learning based error prediction approach for coarse-grid computational fluid dynamics (CG-CFD). *Progress in Nuclear Energy*, 118:103140.

Hassan, M. E., Bourgeois, J., and Martinuzzi, R. (2015). Boundary layer effect on the vortex shedding of wall-mounted rectangular cylinder. *Experiments in Fluids*, 56:33.

Hassan, S., Molla, M. M., Nag, P., Akhter, N., and Khan, A. (2022). Unsteady RANS simulation of wind flow around a building shape obstacle. *Building Simulation*, 15:291–312.

Hemmati, A., Wood, D. H., and Martinuzzi, R. J. (2018). On simulating the flow past a normal thin flat plate. *Journal of Wind Engineering and Industrial Aerodynamics*, 174:170–187.

Hemmati, A., Wood, D. H., and Martinuzzi, R. J. (2019). Wake dynamics and surface pressure variations on two-dimensional normal flat plates. *AIP Advances*, 9:045209.

Hintea., D., Brusey., J., and Gaura., E. (2015). A study on several machine learning methods for estimating cabin occupant equivalent temperature. In *Proceedings of the 12th International Conference on Informatics in Control, Automation and Robotics - Volume 1: ICINCO,*, pages 629–634. INSTICC, SciTePress.

Hochreiter, S. and Schmidhuber, J. (1997). Long Short-Term Memory. *Neural Computation*, 9(8):1735–1780.

Hoffman, G. H. (1975). Improved form of the low reynolds number $k - \epsilon$ turbulence model. *The Physics of Fluids*, 18(3):309–312.

Hosseini, Z., Bourgeois, J. A., and Martinuzzi, R. J. (2013). Large-scale structures in dipole and quadrupole wakes of a wall-mounted finite rectangular cylinder. *Experiments in Fluids*, 54:1595.

Huang, J.-C., Ko, K.-M., Shu, M.-H., and Hsu, B.-M. (2020). Application and comparison of several machine learning algorithms and their integration models in regression problems. *Neural Computing and Applications*, 32:5461–5469.

Huijing, J. P., Dwight, R. P., and Schmelzer, M. (2021). Data-driven RANS closures for three-dimensional flows around bluff bodies. *Computers & Fluids*, 225:104997.

Hwang, J.-Y. and Yang, K.-S. (2004). Numerical study of vortical structures around a wall-mounted cubic obstacle in channel flow. *Physics of Fluids*, 16(7):2382–2394.

Ikhennicheu, M., Druault, P., Gaurier, B., and Germain, G. (2020). Turbulent kinetic energy budget in a wall-mounted cylinder wake using piv measurements. *Ocean Engineering*, 210:107582.

Jones, W. and Launder, B. (1972). The prediction of laminarization with a two-equation model of turbulence. *International Journal of Heat and Mass Transfer*, 15:301–314.

Jones, W. and Launder, B. (1973). The calculation of low-reynolds-number phenomena with a two-equation model of turbulence. *International Journal of Heat and Mass Transfer*, 16(6):1119–1130.

Joubert, E., Harms, T., and Venter, G. (2015). Computational simulation of the turbulent flow around a surface mounted rectangular prism. *Journal of Wind Engineering and Industrial Aerodynamics*, 142:173–187.

Kavian Nezhad, M. R., Lange, C. F., and Fleck, B. A. (2022). Performance evaluation of the RANS models in predicting the pollutant concentration field within a compact urban setting: Effects of the source location and turbulent schmidt number. *Atmosphere*, 13(7).

Kolmogorov, A. N. (1941). The local structure of turbulence in incompressible viscous fluid for very large reynolds numbers. *Cr Acad. Sci. URSS*, 30:301–305.

Konstantinidis, E. and Bouris, D. (2012). Bluff body aerodynamics and wake control. In Lerner, J. C. and Boldes, U., editors, *Applied Aerodynamics*, chapter 4. IntechOpen, Rijeka.

Krajnović, S. (2011). Flow around a tall finite cylinder explored by large eddy simulation. *Journal of Fluid Mechanics*, 676:294–317.

Kuethe, A. M. and Chow, C.-Y. (1997). *Foundations of aerodynamics: bases of aerodynamic design*. John Wiley & Sons.

Lin, P., Hu, G., Li, C., Li, L., Xiao, Y., Tse, K., and Kwok, K. (2021). Machine learning-based prediction of crosswind vibrations of rectangular cylinders. *Journal of Wind Engineering and Industrial Aerodynamics*, 211:104549.

Ling, J., Kurzawski, A., and Templeton, J. (2016). Reynolds averaged turbulence modelling using deep neural networks with embedded invariance. *Journal of Fluid Mechanics*, 807:155–166.

Liu, Y., Guan, X., and Xu, C. (2017). A production limiter study of SST-SAS turbulence model for bluff body flows. *Journal of Wind Engineering and Industrial Aerodynamics*, 170:162–178.

Luo, S., Vellakal, M., Koric, S., Kindratenko, V., and Cui, J. (2020). Parameter identification of RANS turbulence model using physics-embedded neural network. In Jagode, H., Anzt, H., Juckeland, G., and Ltaief, H., editors, *High Performance Computing*, pages 137–149, Cham. Springer International Publishing.

Lübcke, H., Schmidt, S., Rung, T., and Thiele, F. (2001). Comparison of LES and RANS in bluff-body flows. *Journal of Wind Engineering and Industrial Aerodynamics*, 89:1471–1485.

Martinuzzi, R. and Tropea, C. (1993). The flow around surface-mounted, prismatic obstacles placed in a fully developed channel flow (data bank contribution). *Journal of Fluids Engineering*, 115:85–92.

McClean, J. F. and Sumner, D. (2014). An experimental investigation of aspect ratio and incidence angle effects for the flow around surface-mounted finite-height square prisms. *Journal of Fluids Engineering*, 136.

Menter, F. R. (1994). Two-equation eddy-viscosity turbulence models for engineering applications. *AIAA Journal*, 32:1598–1605.

Minsky, M. and Papert, S. (1969). *Perceptrons; an introduction to computational geometry.* MIT Press.

Mohamed, M. and Wood, D. (2017). Modifications to reynolds-averaged navier–stokes turbulence models for the wind flow over buildings. *International Journal of Sustainable Energy*, 36(3):225–241.

Moin, P. and Mahesh, K. (1998). Direct numerical simulation: A tool in turbulence research. *Annual Review of Fluid Mechanics*, 30(1):539–578.

More, B. S., Dutta, S., Chauhan, M. K., and Gandhi, B. K. (2015). Experimental investigation of flow field behind two tandem square cylinders with oscillating upstream cylinder. *Experimental Thermal and Fluid Science*, 68:339–358.

Moukalled, F., Mangani, L., and Darwish, M. (2015). *The Finite Volume Method in Computational Fluid Dynamics: An Advanced Introduction with OpenFOAM and Matlab*. Springer Publishing Company, Incorporated, 1st edition.

Murakami, S. (1993). Comparison of various turbulence models applied to a bluff body. *Journal of Wind Engineering and Industrial Aerodynamics*, 46-47:21–36.

Nakagawa, S., Nitta, K., and Senda, M. (1999). An experimental study on unsteady turbulent near wake of a rectangular cylinder in channel flow. *Experiments in Fluids: Experimental Methods and their Applications to Fluid Flow*, 27(3):284 – 294.

Ng, A. (2020). Coursera: Machine learning.

Nguyen, V., Nguyen-Thoi, T., and Duong, V. (2021). Characteristics of the flow around four cylinders of various shapes. *Ocean Engineering*, 238:109690.

Okajima, A., Nagahisa, T., and Rokugou, A. (1990). A numerical analysis of flow around rectangular cylinders. *Nihon Kikai Gakkai Ronbunshu, B Hen/Transactions of the Japan Society of Mechanical Engineers, Part B*, 56(522):280–288 – 288.

Okamoto, S., Matsunaga, K., and Sunabashiri, Y. (1990). Vortex shedding and turbulent wake from a square cylinder of finite length placed on a ground plane. *Transactions of the Japan Society of Mechanical Engineers ENGINEERS Series B*, 56:2291–2299.

OpenCFD, O. (2019). The open source computational fluid dynamics (CFD) toolbox.

Pope, S. B. (2000). *Turbulent flows.* Cambridge University Press.

Porteous, R., Moreau, D. J., and Doolan, C. J. (2017). The aeroacoustics of finite wall-mounted square cylinders. *Journal of Fluid Mechanics*, 832:287–328.

Ranganathan, A. (2004). The levenberg-marquardt algorithm. *Tutorial on LM algorithm*, 11(1):101–110.

Rastan, M., Shahbazi, H., Sohankar, A., Alam, M. M., and Zhou, Y. (2021). The wake of a wall-mounted rectangular cylinder: Cross-sectional aspect ratio effect. *Journal of Wind Engineering and Industrial Aerodynamics*, 213:104615.

Rastan, M. R., Sohankar, A., and Alam, M. M. (2017). Low-reynolds-number flow around a wall-mounted square cylinder: Flow structures and onset of vortex shedding. *Physics of Fluids*, 29:103601.

Reif, B. P. and Durbin, P. (2011). *Statistical theory and modeling for turbulent flows*. John Wiley & Sons.

Rodi, W. (1997). Comparison of LES and RANS calculations of the flow around bluff bodies. *Journal of Wind Engineering and Industrial Aerodynamics*, 69-71:55–75.

Rosenblatt, F. (1958). The perceptron: a probabilistic model for information storage and organization in the brain. *Psychological review*, 65(6):386.

Roy, C., Blottner, F., and Payne, J. (2003). Bluff-body flow simulations using hybrid RANS/LES. *33rd AIAA Fluid Dynamics Conference and Exhibit*.

Rumelhart, D., Williams, R., and Hinton, G. (1986). Learning representations by back-propagating errors. *Nature*, 323(6088):533–536 – 536.

Saeedi, M., LePoudre, P. P., and Wang, B.-C. (2014). Direct numerical simulation of turbulent wake behind a surface-mounted square cylinder. *Journal of Fluids and Structures*, 51:20–39.

Saeedi, M. and Wang, B.-C. (2016). Large-eddy simulation of turbulent flow around a finite-height wall-mounted square cylinder within a thin boundary layer. *Flow, Turbulence and Combustion*, 97:513–538.

Saha, A. K. (2013). Unsteady flow past a finite square cylinder mounted on a wall at low reynolds number. *Computers & Fluids*, 88:599–615.

Sakamoto, H. and Arie, M. (1983). Vortex shedding from a rectangular prism and a circular cylinder placed vertically in a turbulent boundary layer. *Journal of Fluid Mechanics*, 126:147–165.

Sang, J., Pan, X., Lin, T., Liang, W., and Liu, G. (2021). A data-driven artificial neural network model for predicting wind load of buildings using GSM-CFD solver. *European Journal of Mechanics - B/Fluids*, 87:24–36.

Sapna, S., Tamilarasi, A., Kumar, M. P., et al. (2012). Backpropagation learning algorithm based on levenberg marquardt algorithm. *Comp Sci Inform Technol (CS and IT)*, 2:393–398.

Sarpkaya, T. and Issa, R. I. (1981). On the behavior of the separation bubble on a flat plate at high angles of attack. *Journal of Fluids Engineering*, 103(4):375–379.

Savory, E. and Driver, J. M. (1994). Reattachment length for flow over a circular cylinder at high angles of attack. *Journal of Fluids and Structures*, 8(1):105–124.

Schmitt, F. G. (2007). About Boussinesq's turbulent viscosity hypothesis: historical remarks and a direct evaluation of its validity. *Comptes Rendus Mécanique*, 335(9):617–627.

Shah, K. B. and Ferziger, J. H. (1997). A fluid mechanicians view of wind engineering: Large eddy simulation of flow past a cubic obstacle. *Journal of Wind Engineering and Industrial Aerodynamics*, 67-68:211–224.

Shimada, K. and Ishihara, T. (2002). Application of a modified k-epsilon model to the prediction of aerodynamic characteristics of rectangular cross-section cylinders. *Journal of Fluids and Structures*, 16(4):465 – 485.

Simpson, R. L. (2001). Junction flows. *Annual Review of Fluid Mechanics*, 33:415.

Singh, A. P., Medida, S., and Duraisamy, K. (2017). Machine-learning-augmented predictive modeling of turbulent separated flows over airfoils. *AIAA Journal*, 55(7):2215–2227.

Sohankar, A., Norberg, C., and Davidson, L. (1998). Low-reynolds-number flow around a square cylinder at incidence: study of blockage, onset of vortex shedding and outlet boundary condition. *International Journal for Numerical Methods in Fluids*, 26(1):39–56.

Sumner, D., Heseltine, J. L., and Dansereau, O. J. P. (2004). Wake structure of a finite circular cylinder of small aspect ratio. *Experiments in Fluids*, 37:720–730.

Sumner, D., Rostamy, N., Bergstrom, D., and Bugg, J. (2017). Influence of aspect ratio on the mean flow field of a surface-mounted finite-height square prism. *International Journal of Heat and Fluid Flow*, 65:1–20.

Tennekes, H. and Lumley, J. L. (1972). *A first course in turbulence.* MIT Press.

Tominaga, Y. (2015). Flow around a high-rise building using steady and unsteady RANS CFD: Effect of large-scale fluctuations on the velocity statistics. *Journal of Wind Engineering and Industrial Aerodynamics*, 142:93–103.

Uffinger, T., Ali, I., and Becker, S. (2013). Experimental and numerical investigations of the flow around three different wall-mounted cylinder geometries of finite length. *Journal of Wind Engineering and Industrial Aerodynamics*, 119:13–27.

Versteeg, H. and Malalasekera, W. (2007). *An Introduction to Computational Fluid Dynamics: The Finite Volume Method*. Pearson Education Limited.

Vita, G., Salvadori, S., Misul, D. A., and Hemida, H. (2020). Effects of inflow condition on RANS and LES predictions of the flow around a high-rise building. *Fluids*, 5:233.

Vold, M. (2017). Three-dimensional numerical modeling of water flow in a rock-blasted tunnel.

Von Kármán, T. (1963). *Aerodynamics*. McGraw-Hill paperbacks : science, mathematics and engineering. McGraw-Hill.

Wang, F. and Lam, K. M. (2019). Geometry effects on mean wake topology and large-scale coherent structures of wall-mounted prisms. *Physics of Fluids*, 31:125109.

Wang, H. F. and Zhou, Y. (2009). The finite-length square cylinder near wake. *Journal of Fluid Mechanics*, 638:453–490.

Wang, H. F., Zhou, Y., Chan, C. K., and Lam, K. S. (2006). Effect of initial conditions on interaction between a boundary layer and a wall-mounted finite-length-cylinder wake. *Physics of Fluids*, 18:065106.

Weller, H. G., Tabor, G., Jasak, H., and Fureby, C. (1998). A tensorial approach to computational continuum mechanics using object-oriented techniques. *Computers in Physics*, 12(6):620–631.

White, F. M. (1991). *Flow, Viscous Fluid*. McGraw Hill, Boston, MA.

Wiener, N. (1965). *Cybernetics or Control and Communication in the Animal and the Machine*, volume 25. MIT press.

Wilcox, D. C. (2006). *Turbulence modeling for CFD*. DCW Industries.

Williamson, C.H.K. (1, . . (1996a). Three-dimensional vortex dynamics in bluff body wakes. *Experimental Thermal and Fluid Science*, 12(2):150–168 – 168.

Williamson, C. (1996b). *Vortex dynamics in the cylinder wake.*, volume 28 of *Annual Review of Fluid Mechanics*. Annual Reviews Inc., Mechanical and Aerospace Engineering, Upson Hall, Cornell University.

Williamson, C. (1997). Advances in our understanding of vortex dynamics in bluff body wakes. *Journal of Wind Engineering and Industrial Aerodynamics*, 71:3 – 32.

Xu, X., Yang, Q., Yoshida, A., and Tamura, Y. (2017). Characteristics of pedestrian-level wind around super-tall buildings with various configurations. *Journal of Wind Engineering and Industrial Aerodynamics*, 166:61–73.

Yakhot, A., Liu, H., and Nikitin, N. (2006). Turbulent flow around a wall-mounted cube: A direct numerical simulation. *International Journal of Heat and Fluid Flow*, 27:994–1009.

Yarlanki, S., Rajendran, B., and Hamann, H. (2012). Estimation of turbulence closure coefficients for data centers using machine learning algorithms. In *13th InterSociety Conference on Thermal and Thermomechanical Phenomena in Electronic Systems*, pages 38–42.

Yu, D., Butler, K., Kareem, A., Glimm, J., and Sun, J. (2013). Simulation of the influence of aspect ratio on the aerodynamics of rectangular prisms. *Journal of Engineering Mechanics*, 139:429–438.

Zargar, A., Tarokh, A., and Hemmati, A. (2021). The steady wake of a wall-mounted rectangular prism with a large-depth-ratio at low reynolds numbers. *Energies*, 14:3579.

Zargar, A., Tarokh, A., and Hemmati, A. (2022). The unsteady wake transition behind a wall-mounted large-depth-ratio prism. *Journal of Fluid Mechanics*, 952:A12.

Zhang, D. (2017). Comparison of various turbulence models for unsteady flow around a finite circular cylinder at Re=20000. *Journal of Physics: Conference Series*, 910:012027.

Zhao, C., Wang, H., Zeng, L., Alam, M. M., and Zhao, X. (2021). Effects of oncoming flow turbulence on the near wake and forces of a 3D square cylinder. *Journal of Wind Engineering and Industrial Aerodynamics*, 214:104674.

Zhao, Y., Akolekar, H. D., Weatheritt, J., Michelassi, V., and Sandberg, R. D. (2020). RANS turbulence model development using CFD-driven machine learning. *Journal of Computational Physics*, 411:109413.

Zheng, X., Montazeri, H., and Blocken, B. (2020). CFD simulations of wind flow and mean surface pressure for buildings with balconies: Comparison of RANS and LES. *Building and Environment*, 173:106747.